

| REPORT DOCUMENTATION PAGE | | | | Form Approved OMB No. 0704-0188 | |
|--------------------------------------------------------------------------------------------------------------------------------------------------------------------------------------------------------------------------------------------------------------------------------------------------------------------------------------------------------------------------------------------------------------------------------------------------------------------------------------------------------------------------------------------------------------------------------------------------------------------------------------------------------------------------------------------------------------------------------------------------------------------------------------------------------------------------------------------------------------------------------------------------------------------------------------------------------------------------------------------------------------------------------------------------------------------------------------------------------------------------------------------------------------------------------------------------------------------------------------------------------------------------------------------------------------------------------------------------------------------------------------------------------------------------------------------------------------------------------------------------------------------------------------------------------------------------------------------------------------------------------------------------------------------------------------------------------------------------------------------------------------------------------------------------------------------------------------------------------------------------------------------------------------------------------------------------------------------------------------------------------------------------------------------------------|-----------------------|--------------------------------|---------------------------------------------------------|-----------------------------------------------------------|-----------------------------------------------------------------|
| <p>Public reporting burden for this collection of information is estimated to average 1 hour per response, including the time for reviewing instructions, searching existing data sources, gathering and maintaining the data needed, and completing and reviewing the collection of information. Send comments regarding this burden estimate or any other aspect of this collection of information, including suggestions for reducing the burden, to Department of Defense, Washington Headquarters Services, Directorate for Information Operations and Reports (0704-0188), 1215 Jefferson Davis Highway, Suite 1204, Arlington, VA 22202-4302. Respondents should be aware that notwithstanding any other provision of law, no person shall be subject to any penalty for failing to comply with a collection of information if it does not display a currently valid OMB control number.</p> <p>PLEASE DO NOT RETURN YOUR FORM TO THE ABOVE ADDRESS.</p> | | | | | |
| 1. REPORT DATE (DD-MM-YYYY) 22-10-2010 | | 2. REPORT TYPE Final Report | | 3. DATES COVERED (From – To) 1 August 2007 - 01-Aug-10 | |
| 4. TITLE AND SUBTITLE Unsteady Lift Generation for MAVs | | | 5a. CONTRACT NUMBER FA8655-07-1-3082 | | |
| | | | 5b. GRANT NUMBER | | |
| | | | 5c. PROGRAM ELEMENT NUMBER | | |
| 6. AUTHOR(S) Dr. Holger Babinsky | | | 5d. PROJECT NUMBER | | |
| | | | 5d. TASK NUMBER | | |
| | | | 5e. WORK UNIT NUMBER | | |
| 7. PERFORMING ORGANIZATION NAME(S) AND ADDRESS(ES) University of Cambridge Trumpington Street Cambridge CB2 1PZ United Kingdom | | | 8. PERFORMING ORGANIZATION REPORT NUMBER N/A | | |
| 9. SPONSORING/MONITORING AGENCY NAME(S) AND ADDRESS(ES) EOARD Unit 4515 BOX 14 APO AE 09421 | | | 10. SPONSOR/MONITOR'S ACRONYM(S) | | |
| | | | 11. SPONSOR/MONITOR'S REPORT NUMBER(S) Grant 07-3082 | | |
| 12. DISTRIBUTION/AVAILABILITY STATEMENT Approved for public release; distribution is unlimited. | | | | | |
| 13. SUPPLEMENTARY NOTES | | | | | |
| 14. ABSTRACT <p>The aim of the current research is to understand unsteady lift generation on three-dimensional flapping wings in the MAV flight regime and, if a leading edge vortex develops at MAV-like Reynolds numbers, characterize the time-scale of the development and stability of the vortex. The waving wing experiment is a model of the translational phase of the insect wing stroke. It was designed to produce a simple flow-field while preserving flow unsteadiness, three-dimensionality, and wing rotation. The wing rotates in a propeller-like motion through a wing stroke angle up to 90 degrees. Unsteady lift and drag force data was acquired throughout the wing stroke and particle image velocimetry (PIV) was used to measure the velocity field and quantify the circulation of the leading edge vortex.</p> <p>The shape of the lift curve was similar for all cases tested. A transient high lift peak approximately 1.5 times the quasi-steady value occurred in the first chord-length of travel, caused by the formation of a leading edge vortex. This vortex then separated from the leading edge resulting in a sharp drop in lift. Subsequent vortices continued to form, shed, and move downstream over the wing as lift values recovered to an intermediate value.</p> <p>The circulation of the LEV has been measured and agrees well with force data. Wing kinematics had only a small effect on the aerodynamic forces produced by the waving wing. In the early stages of the wing stroke, velocity profiles with low accelerations affected the timing and magnitude of the lift peak but at higher accelerations the velocity profile was insignificant. Variations in angle of attack between 5 and 45 degrees, Reynolds number between 10,000 and 60,000, and aspect ratio 2 or 4 did not affect the fundamental structure of the flow. Unlike previous studies at much lower Reynolds numbers, there is no evidence of an attached leading edge vortex over an extended period of time.</p> | | | | | |
| 15. SUBJECT TERMS EOARD, Aerodynamics, Micro Air Vehicle, Aeroelasticity | | | | | |
| 16. SECURITY CLASSIFICATION OF: | | | 17. LIMITATION OF ABSTRACT UL | 18. NUMBER OF PAGES 35 | 19a. NAME OF RESPONSIBLE PERSON Gregg Abate |
| a. REPORT UNCLAS | b. ABSTRACT UNCLAS | c. THIS PAGE UNCLAS | | | 19b. TELEPHONE NUMBER (Include area code) +44 (0)1895 616021 |

WAVING WING AERODYNAMICS AT LOW REYNOLDS NUMBERS

H. BABINSKY AND A. R. JONES

UNIVERSITY OF CAMBRIDGE
UNITED KINGDOM

EOARD CONTRACT FA 8655-07-1-3082

**FINAL REPORT
JULY 2010**

ABSTRACT

In recent years aeronautical research has focused on the development of small remotely controlled micro air vehicles (MAVs). MAVs will operate at low Reynolds numbers $O(10^4)$, below the domain of traditional aerodynamics but well above the regime of insect flight. At Reynolds number $O(10^5)$ lift is generated via steady attached flow but flow tends to separate easily and wings are limited to low angles of attack. In the insect flight regime, Reynolds number $O(10^3)$, a stable leading edge vortex (LEV) is thought to be responsible for high lift on flapping wings at high angles of attack. It is not yet known whether such a vortex develops at Reynolds numbers typical of MAVs and to what extent three-dimensionality is necessary to sustain it. The aim of the current research is to understand unsteady lift generation on three-dimensional flapping wings in the MAV flight regime and, if a leading edge vortex develops at MAV-like Reynolds numbers, characterize the time-scale of the development and stability of the vortex.

The waving wing experiment is a model of the translational phase of the insect wing stroke. It was designed to produce a simple flow-field while preserving flow unsteadiness, three-dimensionality, and wing rotation. The wing rotates in a propeller-like motion through a wing stroke angle up to 90 degrees. Unsteady lift and drag force data was acquired throughout the wing stroke and particle image velocimetry (PIV) was used to measure the velocity field and quantify the circulation of the leading edge vortex.

The shape of the lift curve was similar for all cases tested. A transient high lift peak approximately 1.5 times the quasi-steady value occurred in the first chord-length of travel, caused by the formation of a leading edge vortex. This vortex then separated from the leading edge resulting in a sharp drop in lift. Subsequent vortices continued to form, shed, and move downstream over the wing as lift values recovered to an intermediate value.

The circulation of the LEV has been measured and agrees well with force data. Wing kinematics had only a small effect on the aerodynamic forces produced by the waving wing. In the early stages of the wing stroke, velocity profiles with low accelerations affected the timing and magnitude of the lift peak but at higher accelerations the velocity profile was insignificant. Variations in angle of attack between 5 and 45 degrees, Reynolds number between 10,000 and 60,000, and aspect ratio 2 or 4 did not affect the fundamental structure of the flow. Unlike previous studies at much lower Reynolds numbers, there is no evidence of an attached leading edge vortex over an extended period of time.

CONTENTS

| | |
|-----------------------------------------|----|
| 1. Introduction | 4 |
| 2. Objectives | 4 |
| 3. Experimental Methods | 5 |
| 3.1. Experimental setup | 5 |
| 3.2. Force measurements | 7 |
| 3.3. Particle image velocimetry | 7 |
| 3.4. Experimental uncertainty | 7 |
| 3.4.1. Wing kinematics | 8 |
| 3.4.2. PIV | 8 |
| 3.4.3. Force measurements | 8 |
| 3.5. Vortex identification | 10 |
| 4. Results and Discussion | 10 |
| 4.1. Flow-Field Around a Waving Wing | 10 |
| 4.1.1. Chordwise Views | 10 |
| 4.1.2. Spanwise Variations | 11 |
| 4.1.3. Spanwise Views | 13 |
| 4.1.4. Force History | 16 |
| 4.1.5. Leading Edge Vortex Circulation | 18 |
| 4.1.6. Three Phases of Flow Development | 20 |
| 4.2. Effect of Wing Kinematics | 21 |
| 4.3. Effect of Angle of Attack | 22 |
| 4.4. Effect of Reynolds Number | 25 |
| 4.5. Effect of Aspect Ratio | 28 |
| 5. Conclusions | 31 |
| Publications | 32 |
| References | 33 |

1. INTRODUCTION

Insect flight has long been the domain of biologists but engineers have recently taken an interest in insect aerodynamics. Unlike an airplane wing which produces lift in an attached steady flow, insects rely on flapping wings to generate lift in separated flow. Recent efforts to develop micro air vehicles (MAVs) have focused on understanding how natural flapping wings generate lift.

At the low Reynolds numbers typical of insect flight, flow is characterized by the formation of a vortex along the leading edge of the wing. An attached leading edge vortex has been observed by multiple research groups on both mechanical wing flappers (8; 22; 21; 4) and revolving wing models (20). The first revolving wing experiments were performed by Usherwood and Ellington (20) at $Re \approx 8,000$. In this setup the wing is rotated about the root in a propeller-like motion, producing a spanwise velocity gradient in a quasi-steady flow. At high angles of attack the flow separates from the leading edge and travels radially towards the wing tip. This separated spanwise flow forms a leading edge vortex.

Spanwise flow was also observed by Ellington et al. (8) in their earlier experiments on the mechanical hawkmoth flapper at $Re \approx 10,000$. In these experiments the spanwise flow observed was comparable to the wingtip speed and was attributed to the velocity gradient along the flapping wing. As on revolving wings, the wingtip moves at a higher velocity than does the wing root and the resulting pressure gradient should induce a spanwise flow. The presence of a strong spanwise flow could stabilize the leading edge vortex much like on a delta wing, by transporting the vorticity towards the wingtip and limiting the growth of the vortex (13; 8; 22; 21).

Birch et al. (4) report that at Reynolds numbers $O(100)$ spanwise flow exists both within the core of the leading edge vortex and behind it, but is relatively weak. Later experiments suggest that this spanwise flow may be induced by the centripetal and Coriolis accelerations present on rotating wings at low Rossby number, taken to be approximately equal to the wing aspect ratio for a revolving wing (12).

At higher Reynolds numbers $O(1,000)$ the structure of the leading edge vortex may be more sensitive. Ellington et al. (8) and Birch et al. (4) both performed experiments on mechanical wing flappers at similar Reynolds numbers, $Re \approx 1,000$ and $1,400$ respectively. Both sets of experiments revealed a stable attached leading edge vortex. At still higher Reynolds numbers, $Re \approx 8,000$, Tarascio et al. (18) observed vortices periodically shedding from a flapping wing, as did Jones and Babinsky (11) at $Re = 60,000$ on a waving wing model.

Many previous studies have modeled insect flight using mechanical flappers (4; 8; 17; 18; 21). Simpler models have isolated either the rotational or translational phase of the wing stroke using a pitching (6; 15) or sliding (1; 19) wing, but these setups neglect the sweeping motion. During the translational phase of an insect wing stroke, this sweeping motion establishes a velocity gradient from wing root to tip which is thought to induce a spanwise flow that stabilizes the leading edge vortex (8). Revolving wing experiments (20; 12) preserve this velocity gradient but neglect the starting and stopping that occurs at the beginning and end of the wing stroke. As an insect wing stroke is only 2 to 5 chord-lengths, these accelerations are expected to have a significant effect on the flow field (5; 7).

Recently, more work has been done on propeller-like revolving wings. CFD simulations have captured the leading edge separation which causes the formation of a leading edge vortex. This vortex remains attached to the leading edge for the first 2 chord-lengths of travel before separating. Force predictions suggest a period of low lift for the first 50 degrees of rotation and quasi-steady state after about 90 degrees of sweep. Experiments show that the lift does not reach steady state until several revolutions have passed, but does plateau near 90 degrees (23).

2. OBJECTIVES

The current research endeavors to shed some light on the development and stability of the leading edge vortex and quantify the lift produced at MAV-like Reynolds numbers. Experiments are performed at a Reynolds number of 60,000, near the MAV target Reynolds number, and

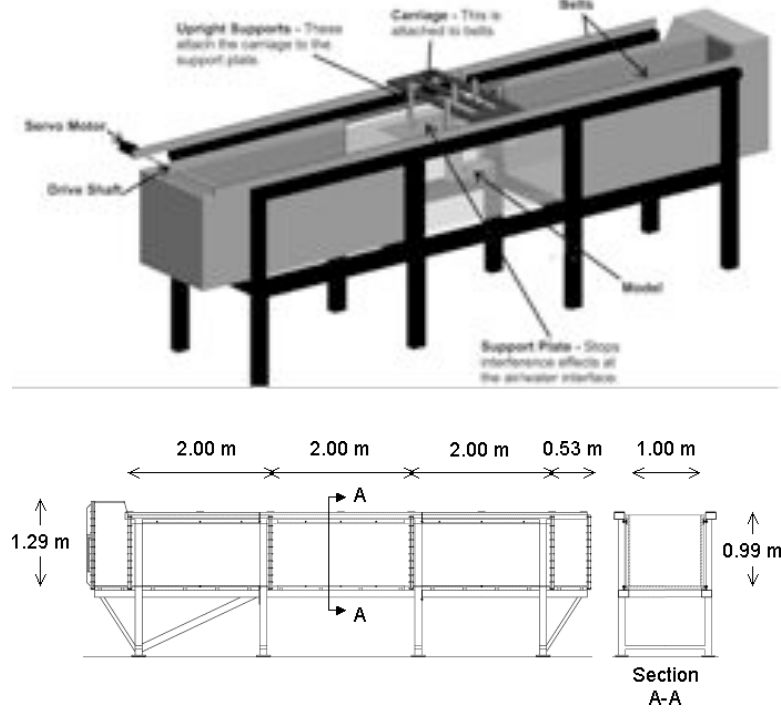


FIGURE 1. CUED towing tank.

extended to a Reynolds number of 10,000 to enable comparisons with previous work done at lower Reynolds numbers. The setup presented here, the waving wing experiment, was developed to produce the simplest flow-field possible while preserving the key features of the insect wing stroke thought to produce a stable leading edge vortex. The objectives of this research are to determine if a stable attached leading edge vortex forms at MAV-like Reynolds numbers and to understand unsteady lift generation in this regime. In particular, the significance of three-dimensional effects and wing acceleration on the development and behavior of this vortex and the resulting unsteady lift are examined. Furthermore, this simple yet fully three-dimensional flow-field provides a canonical test case for CFD validation.

3. EXPERIMENTAL METHODS

3.1. Experimental setup. The waving wing experiment is a fully three-dimensional simplification of the flapping wing motion observed in nature. The spanwise velocity gradient and wing starting and stopping acceleration that exist on an insect-like flapping wing are generated by rotational motion of a finite span wing. This setup preserves key features of the wing stroke which are neglected in other models while the simple geometry allows identification of fundamental structures in the flow. The wing is started from rest and swept through a stroke angle θ up to 85 degrees. The time-history of the angular velocity of the wing is fully programmable.

Experiments were performed by waving a wing through water in the Cambridge University Engineering Department (CUED) towing tank, shown in Figure 1. By using water as the working medium it is possible to achieve the required Reynolds numbers with relatively slow motions and a large model, providing an optimal environment for high resolution data acquisition in both time and space. The towing tank is 7 m long and has a $1 \text{ m} \times 1 \text{ m}$ cross-section with a central 2 m long Perspex test section and a glass window on one end. A sketch and photo of the waving wing mechanism is shown in Figure 2. The entire setup is shown suspended from the towing tank carriage on four vertical struts and the Perspex sides and water volume of the tank are shown to provide a sense of scale. The water depth is 0.8 m.

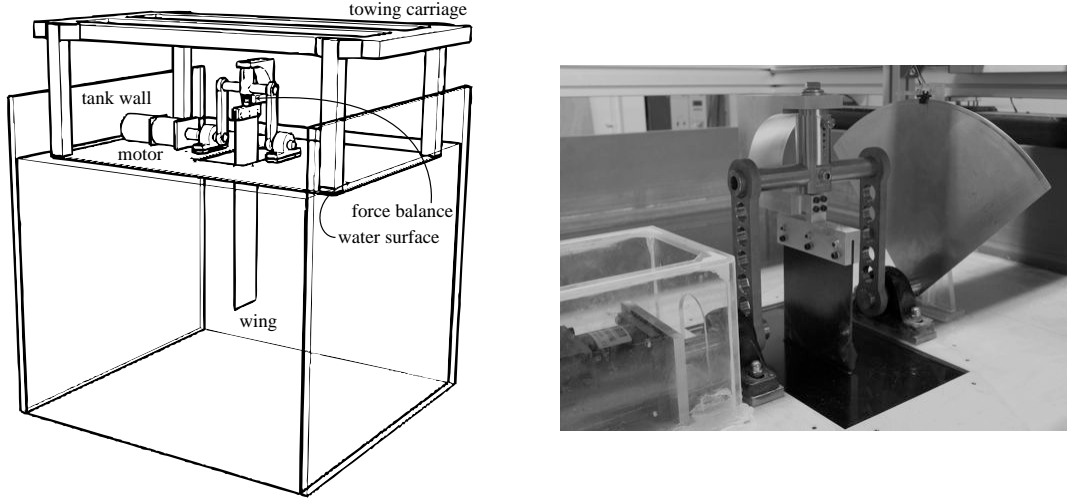


FIGURE 2. The waving wing mechanism.

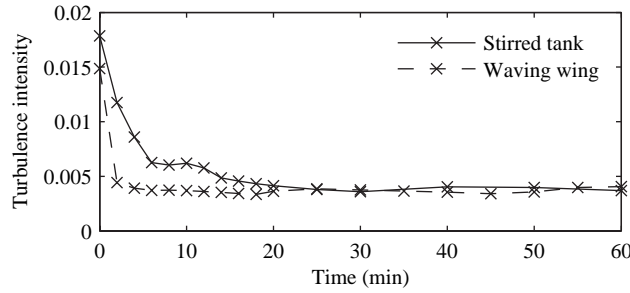


FIGURE 3. Decay of turbulence intensity with time.

The waving motion is controlled by a servomotor and gearbox programmable through Lab-View, and a slotted optical switch is mounted near one end of the axle to confirm wing position. A force balance can be mounted on the wing to provide unsteady lift and drag force measurements. The distance from the wing root (defined as the bottom of the skim plate when the wing is vertical) to the axis of rotation is 10% of the wing span, similar to previous propeller experiments (14). The angle of attack is selectable from 0 to 45 degrees in 5 degree increments. The wing is a 2.5% thick carbon fiber flat plate with rounded edges, a chord of 0.125 m, and an aspect ratio of 4. An 85 degree wing stroke is equivalent to 5.07 chord-lengths of travel at 3/4 span of the aspect ratio 4 wing. Blockage of the towing tank is 5.5% for a 45 degree angle of attack.

Particle image velocimetry (PIV) was used to study the turbulence intensity in the towing tank. The tank was allowed to settle overnight then a disturbance was introduced: the tank was stirred as when mixing in seeding particles for PIV, or the waving arm mechanism was moved as for a wing stroke. The velocity field was measured at set times past the disturbance. The turbulence intensity, shown in Figure 3, was calculated up to two hours past the disturbance and again overnight, never dropping below about 0.4%. This suggests that the actual turbulence is likely to be lower than that value but measurements are limited by the capabilities of the PIV system. Based on these results, the tank was allowed to settle for 30 minutes after mixing in PIV particles and 10 minutes between wing strokes.

The wing stroke was programmed using a linear velocity profile in time as shown in Figure 4. The wing was accelerated such that it reached its maximum velocity after 0.25 chord-lengths of travel. The velocity profile was symmetric such that the wing decelerated in the same way

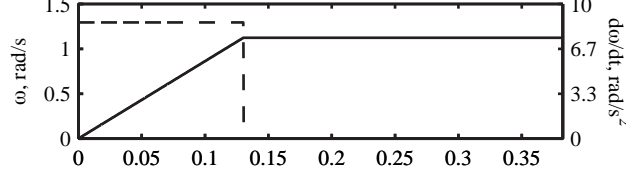


FIGURE 4. Commanded wing kinematics for first quarter-stroke accelerating over 0.25c: angular velocity (solid) and acceleration (dashed) as a function of time.

before reaching the end of the stroke. The maximum velocity was chosen as that which gives the target local wing Reynolds number at 3/4 span.

3.2. Force measurements. A water-resistant force balance has been designed and fabricated. The force balance is capable of measuring two force components to 10 N with a resolution of at least 0.01 N. When paired with a Fylde FE-379-TA transducer amplifier and National Instruments USB-6221 Multifunction DAQ, unsteady lift and drag forces can be measured at frequencies up to 250 kHz.

Two-component force balance measurements were sampled at 7 kHz in both air and water for the wing waving through 85 degrees. The force balance was mounted such that it measured the forces normal and tangential to the wing and the measured forces were rotated by the angle of attack to compute lift and drag. Because the tangential force is much smaller than the normal force, both the lift and drag forces are dominated by the force normal to the plate. Wing lift and drag coefficients were obtained by subtracting the inertial forces measured in air from the forces measured in water, subtracting the buoyancy forces, and normalizing by the local wing velocity. Lift and drag coefficients are given by

$$(1) \quad C_L = \frac{6L}{\rho\omega^2 c(r_t^3 - r_r^3)}$$

$$(2) \quad C_D = \frac{6D}{\rho\omega^2 c(r_t^3 - r_r^3)},$$

where r_t and r_r are the distances from the axis of rotation to the wing tip and wing root. Force data was averaged over five runs.

3.3. Particle image velocimetry. Particle image velocimetry was performed using a LaVision FlowMaster 4S DPIV with a high resolution high speed camera capable of up to 1000 frames per second at a resolution of 1024×1024 pixels and a Nd:YLF double cavity laser.

To obtain PIV data for chordwise slices of the waving wing the laser sheet was oriented horizontally and entered the tank through the side wall. The camera was placed below the tank as shown in Figure 5. Images were taken at 1/4, 1/2, 3/4, and 7/8 span throughout the wing stroke. Each case was repeated between 5 and 50 times though analysis of early data demonstrated that 5 runs was sufficient in all cases.

Vestosint 7182 particles with a specific gravity of 1.02 were used to seed the flow and appeared in the images with a diameter of 2 to 3 pixels. Images were taken at frame rates between 50 and 750 Hz at a resolution of 1024×1024 pixels with a 20×20 cm or 35×35 cm field of view. Frame rates were chosen for a 3 to 5 pixel particle displacement within image pairs. PIV images were processed in two passes with interrogation windows decreasing from 32×32 to 16×16 pixels with Gaussian weighting and 50% overlap. The average velocity field was obtained by averaging the velocity components at each spatial point for the 5 runs.

3.4. Experimental uncertainty.

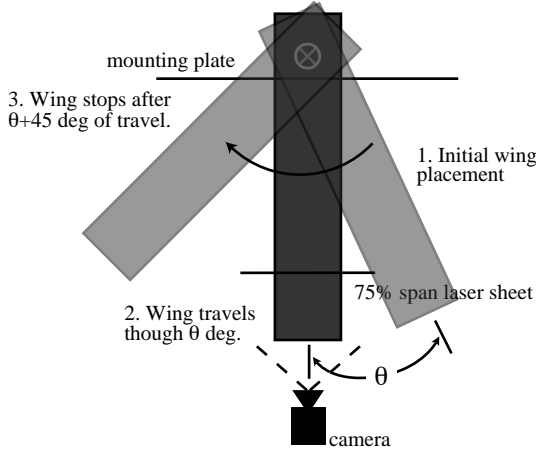


FIGURE 5. Chordwise PIV setup.

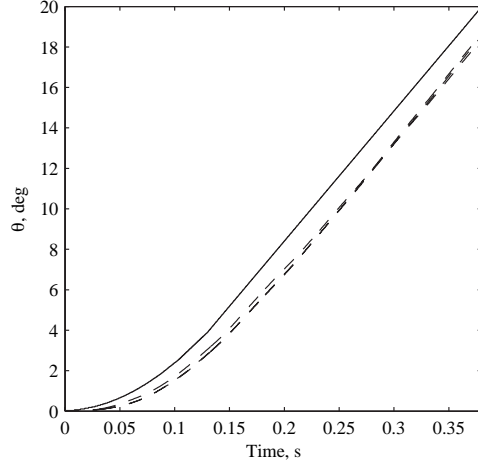


FIGURE 6. Commanded (solid) and measured (dashed) wing position for the first quarter of the wing stroke at $Re = 60,000$.

3.4.1. *Wing kinematics.* The wing angle of attack is accurate to within $1/60$ of a degree and the position to within 0.2 degrees or 0.06 mm at $3/4$ span. The wing position as a function of time was measured using a high speed camera. Images were acquired at 2 kHz and the angular position of the wing computed for three runs. Figure 6 shows the angular wing position as a function of time for the wing at a 45 degree angle of attack and $Re = 60,000$. There are three sets of dashed lines representing the three runs measured. Once the wing has reached its constant velocity there is a 10% error in position or a 3.5% error in angular velocity. The error in wing position appears to be due to a slight delay in the start of the wing motion, thus despite the offset the wing position at a given point in time is precise.

3.4.2. *PIV.* The total error for the PIV measurements, $\epsilon_{tot} = \epsilon_{bias} + \epsilon_{rms}$, was first estimated using the trends and values reported in the literature. For the current PIV setup, $\epsilon_{bias} \approx -0.01$ due to the loss of pixels (16). The random error can be expressed as the sum of the uncertainty due to particle image diameter of 3 pixels, displacement between 1 and 3 pixels, and density averaging 8 particles per window: $\epsilon_{rms} = 0.009 + 0.01 + 0.025 = \pm 0.04$. The total error becomes $\epsilon_{tot} = +0.03 / -0.05$ pixels. Error was also estimated by evaluating PIV images with a known displacement. An artificial image was generated with an average of fifteen 3-pixel particles per 16×16 interrogation widow. This image was displaced by 1, 2, 3, or 4 pixels and evaluated with the LaVision DaVis 7.2 software. The RMS error for these images with constant displacement was ± 0.01 of a pixel. To account for the error due to imperfect particle image shapes, intensities, and image noise, real images of the waving wing were artificially displaced and evaluated. The RMS error for these images was 0.03 of a pixel, or 1.7% of the displacement. This value agrees well with the value estimated from the literature. Calibration error is approximately 0.2 pixels and the total error at $Re = 30,000$ is approximately 0.029 ms^{-1} .

3.4.3. *Force measurements.* The RMS and bias error are given in Table 1 for both the force signal and the force coefficient. The waving wing rig was observed to vibrate at a frequency near 20 Hz in both air and water when the stepper motor is run with and without the wing attached. This vibration appears in the force measurements at all Reynolds numbers. The signal noise is dominated by a high frequency electrical noise above 100 Hz which tends to be stronger as Reynolds number decreases. At lower Reynolds numbers the stepper motor controlling the

TABLE 1. Uncertainty in Force Measurements.

| | Force, N | | Force Coefficient | |
|-------------|----------|------------|-------------------|------------|
| | Normal | Tangential | Normal | Tangential |
| Re = 60,000 | | | | |
| RMS | 0.41 | 0.81 | 0.09 | 0.18 |
| Bias error | 0.10 | 0.06 | 0.02 | 0.01 |
| Re = 30,000 | | | | |
| RMS | 0.56 | 0.43 | 0.51 | 0.39 |
| Bias error | -0.04 | 0.01 | -0.04 | 0.01 |
| Re = 10,000 | | | | |
| RMS | 0.32 | 0.26 | 2.35 | 2.38 |
| Bias error | 0.04 | -0.05 | 0.45 | -0.23 |

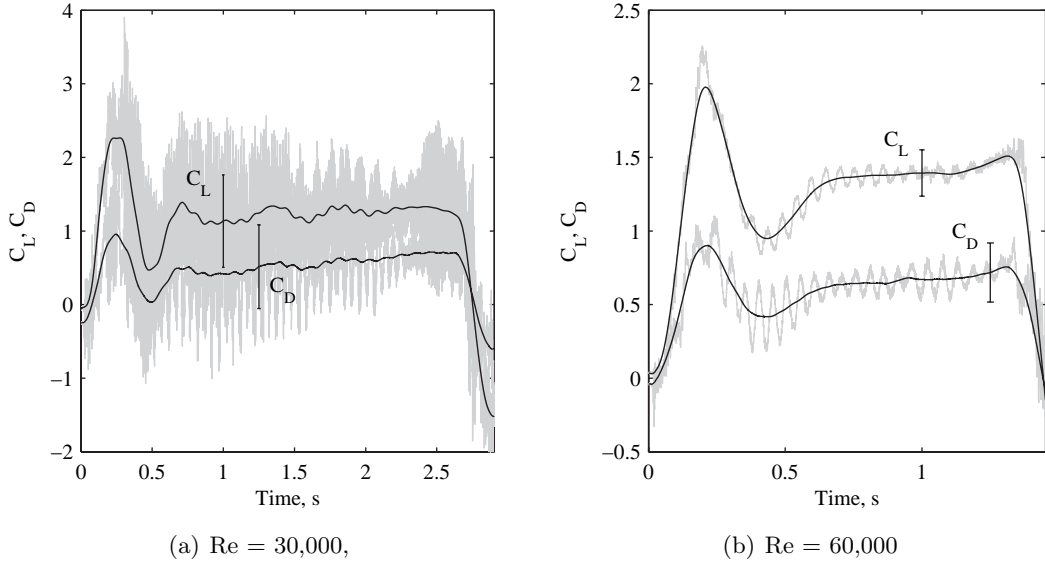


FIGURE 7. Force coefficients at $\alpha = 25$ deg.

waving motion operates at a lower angular velocity and the motor steps become more distinct, exciting the resonance frequency of the rig and amplifying the high frequency noise.

Some of the force data presented later is shown as a smoothed curve for clarity. A moving average over 400 samples of 0.06 s was applied to the raw force signal. Approaching the ends of the signal, the averaging window shrinks and errors can be larger in those regions, but in general the smoothed signal preserves the shape of the curves well and makes comparisons much clearer. Examples of the unsteady lift and drag coefficients at a 25 degree angle of attack is given in Figure 7 for $Re = 30,000$ and $60,000$. The raw data is shown in grey and smoothed signal is given by the solid black line. Error bars represent the RMS error in the force coefficients. At both Reynolds numbers there is steep lift peak very early on in both the raw and the smoothed signal as well as a dip due to inertial forces near the end of the stroke. The force peaks are much larger in the raw signal than in the smoothed and it is impossible to tell if this is due to vibration or an aerodynamic force, but the difference in magnitude of the lift peak is within the experimental error.

Forces acting on the wing produce a significant bending moment at the balance. The effect of this bending moment was found by placing a weight a known distance away from the center of the force balance in each direction. A moment correction was then determined by estimating the center of force on the wing and computing the quasi-steady moment applied to the force

balance in each channel. The moment correction is approximately a -9% change in the lift coefficient and a +6% change in the drag coefficient.

3.5. Vortex identification. In the highly separated unsteady flow that develops over the waving wing, it is useful to identify the vortices present in order to track their development. The most common approach is to directly compute the vorticity field by taking the curl of the velocity field obtained through PIV. The vorticity normal to the light sheet is

$$\omega_z = \frac{\partial v}{\partial x} - \frac{\partial u}{\partial y}$$

where the derivatives can be approximated using a central differencing scheme such that

$$\left(\frac{df}{dx}\right)_i \approx \frac{f_{i+1} - f_{i-1}}{2\Delta x}$$

and an area of the flow field with a high vorticity value can be considered a vortex. This method presents two difficulties. Although some methods are better suited for PIV data than others, differentiating the velocity measurements amplifies noise in the velocity measurements. Also, since the magnitude of the vorticity can be comparable, it can be difficult to identify vortices in a shear flow, thus vorticity alone is not a sufficient condition for vortex identification (10).

A non-local vortex detection scheme developed by (9) was also used. This algorithm considers the topology of the velocity field rather than the magnitude. A scalar function γ at point P is defined as

$$\gamma(P) = \frac{1}{N} \sum_S \sin(\theta_M)$$

where S is a two-dimensional area centered on point P and N is the number of points inside S . θ_M is the angle between the radius vector from P to a point M that lies on S and the relative velocity vector at M , the total velocity at the point M minus the average velocity across the area S . γ is at its maximum when P is at the center of an axisymmetric vortex and is a measure of the vortex strength. (9) defined a vortex core as the area within a $|\gamma| = 0.6$ contour.

In a typical flow over the waving wing, flow separates at the sharp leading edge forming a shear layer. As vorticity is continuously generated at the leading edge, this shear layer grows and discrete vortices break off and convect downstream. The time-resolved PIV data reveals a trail of vortices shedding from the leading edge and the time at which these vortices separate from the leading edge is of primary interest. Vortex break-off (or shedding) occurs when a region of vorticity splits into two vortex cores. In practice, the $\gamma = 0.6$ contour often encloses two smaller cores of higher vorticity and in the current work the break-off point is defined as the point at which two separate regions of $\gamma = 0.8$ appear. By this definition, the vortex break-off point is highly sensitive to the resolution of the velocity data and the computed vortex break-off point for data taken at different resolutions is not comparable..

4. RESULTS AND DISCUSSION

A detailed analysis of the flow around a waving wing with aspect ratio 4 at a 15 degree angle of attack and Reynolds number 60,000 is presented first. The effects of varying wing kinematics, angle of attack, Reynolds number, and aspect ratio are summarized in the following sections.

4.1. Flow-Field Around a Waving Wing.

4.1.1. Chordwise Views. Figure 8 shows chordwise slices of the normalized vorticity and γ function distributions in the flow-field for several points throughout the wing stroke of a waving wing with aspect ratio 4 at a 15 degree angle of attack and Reynolds number 60,000. Each row of images shows four spanwise locations on the wing (1/4, 1/2, 3/4, and 7/8 span) at a constant wing stroke angle θ with the wing moving from right to left. For each view, the vorticity field was computed by taking the curl of the velocity field as measured using PIV. The results are then normalized by the wing chord and local wing velocity at the spanwise plane of interest and

values outside of the experimental error are shown. The colors are normalized across all of the figures for easier comparison.

A vortex forms along the leading edge of the wing within the first 10 degrees of the wing stroke. This leading edge vortex soon separates from the wing and moves downstream over the upper surface of the wing while a second vortex forms. Subsequent leading edge vortices continue to shed, forming a line of vortices above the wing.

The frequency of the vortex shedding can be found by plotting the vortex strength at a fixed point on the wing as a function of time. Figure 9 shows the maximum $|\gamma|$ on a vertical line passing through the quarter-chord of the wing. The absolute value of γ is plotted, so a large $|\gamma|$ represents a strong vortex even though the leading edge vortices have a negative γ value. Snapshots of the flow-field at four points in time are given in (a-d). In (a) a strong vortex is centered on the quarter-chord and the maximum $|\gamma|$ value is large. The flow-field at (b) is an example of the flow when the maximum $|\gamma|$ value dips below 0.6 and there is no vortex present at the quarter-chord. In (c) the vortex centered on the quarter-chord is weaker than the previous shed vortices, but is still a distinct vortex. Later in the wing stroke at (d) the vortex strength increases again as vortices continue to shed from the leading edge. The amplitude spectrum of the signal shows that the vortex shedding frequency is approximately 18 Hz.

Also of interest is the speed at which the shed vortices move downstream. Figure 10 shows the streamwise position of the first leading edge vortex after it has separated from the wing. Also shown is the position of the leading edge of the wing moving at a constant velocity of 0.48 ms^{-1} . Figures (a-c) show contours of γ at two instants 0.07 seconds apart as marked by the vertical dotted lines. The earlier time is shown in grey and the later one in black. The shed LEV moves forward more slowly than the wing does and thus the distance between the vortex and leading edge increases. In a wing-fixed frame of reference, the shed vortex appears to move downstream and pass over the upper surface of the wing. Between $t = 0.26$ and 0.64 seconds, the vortex is over the wing as shown in (a) and (b). During this time the vortex moves approximately 0.27 ms^{-1} slower than the wing. Near the trailing edge, the shed vortices tend to merge into one and the vortex slows down even further as shown in (c). The speed of the vortex asymptotically approaches the freestream speed and so appears stationary in the inertial reference frame.

All of the images of the flow-field that have been shown thus far are instantaneous snapshots intended to resolve the unsteady structures in the flow-field. Figure 11 shows the flow-field at $3/4$ span time-averaged over 0.48 seconds. This corresponds to 30.8 degrees of the wing stroke from approximately 1.9 to 3.6 chord-lengths traveled. In this time-averaged view the trail of vortices is no longer visible and the wing appears to be in deep stall with a large region of separated flow extending over the entire length of the chord.

4.1.2. Spanwise Variations. Despite the highly three-dimensional nature of the waving wing experiment, the fundamental structure of the flow is very similar along the wing span (Fig. 8). The vortices that form at the leading edge extend along the entire length of the wing.

Looking more closely at the vorticity fields in Section 4.1.1, Figure 8, there are two differences in the behavior of the leading edge vortices along the span. The first is the height of the shed vortices. The shed vortices appear to lift off the wing surface more quickly on the outboard sections of the wing. This is most apparent in Figures 8(e-h), all at a stroke angle of $\theta = 27.63$ degs. At this point in the wing stroke, the first shed vortex is clearly near the wing surface at $1/4$ and $1/2$ span, but has lifted almost a core-diameter above the wing surface at $7/8$ span.

Secondly, shed leading edge vortices spread farther apart on the outboard sections. For example, four vortices are observed over the wing at a wing stroke angle $\theta = 50.85$ deg. These four vortices cover approximately half of the wing chord at $1/2$ span. The same number of vortices stretch across $3/4$ of the chord at $3/4$ span and the vorticity extends past the trailing edge at $7/8$ span. This could be because the wing tip has moved significantly farther than the wing root in terms of absolute distance. At a stroke angle of 50.85 degrees the $1/2$ span plane has traveled only 2.15 chord-lengths whereas the $7/8$ span plane has traveled 3.48 chord-lengths.

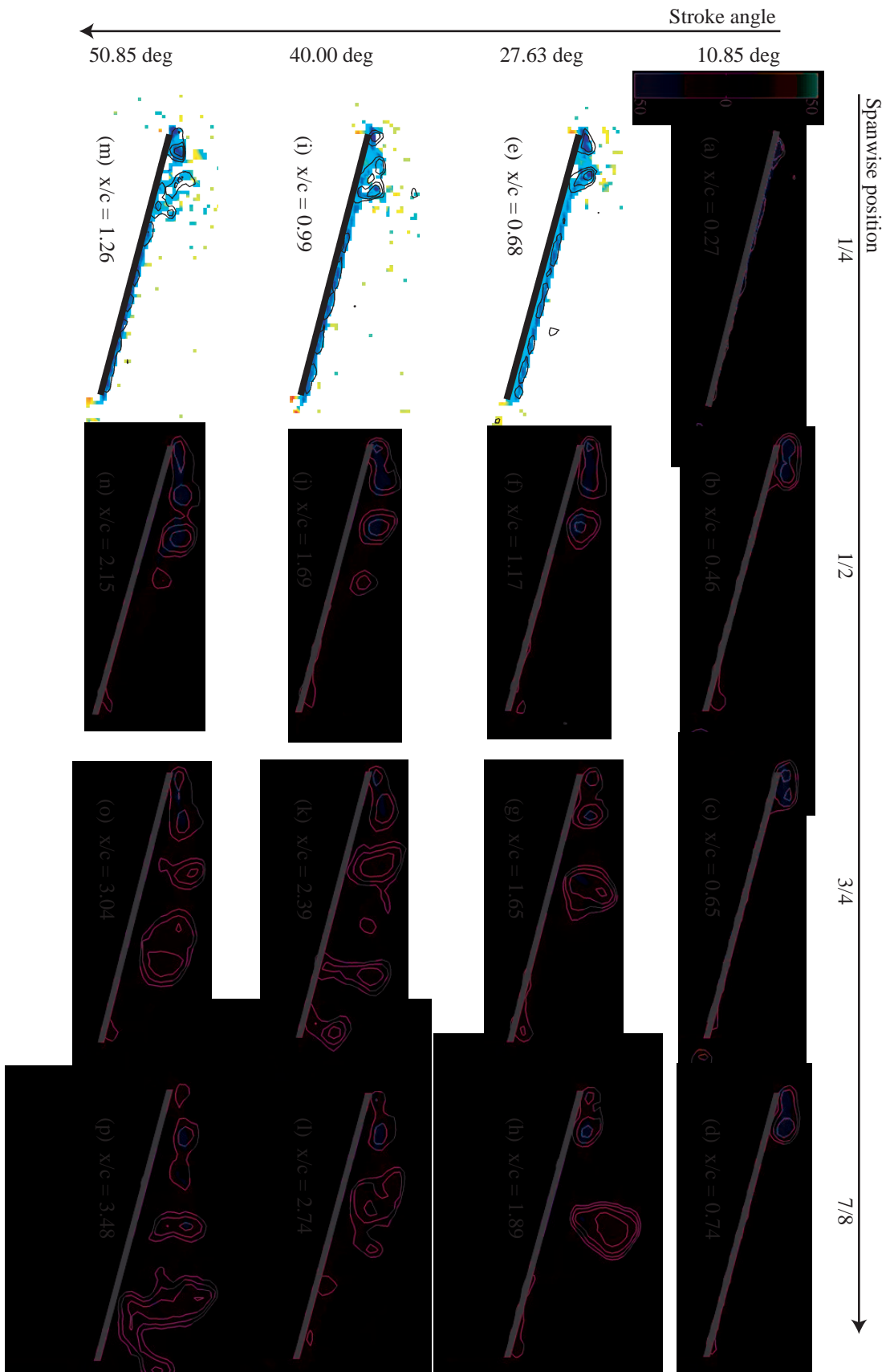


FIGURE 8. Normalized vorticity fields. Each row represents the four stations on the wing at an instant in the wing stroke.

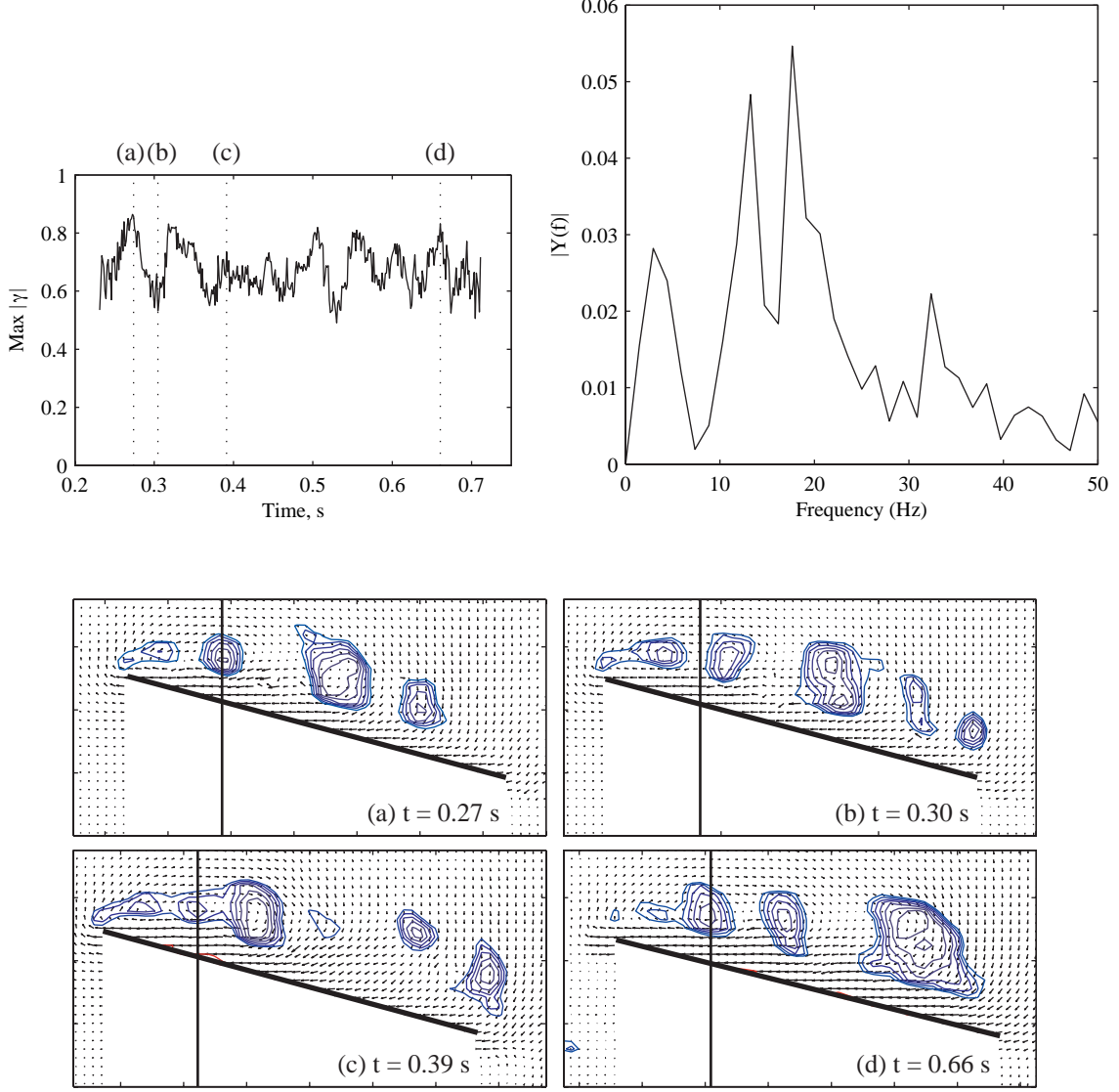


FIGURE 9. Vortex shedding at 3/4 span.

Figure 12 shows the flow-field at three locations, this time after traveling the same absolute distance. The first row of images shows the 1/2, 3/4, and 7/8 span planes each having traveled 0.69 chord-lengths, thus the 1/2 span plane has passed through a wing stroke angle of 16.34 degrees whereas the 7/8 span plane has passed through only 10.09 degrees. In this frame of reference the shed vortices are spread along the same streamwise distance at the different spanwise locations, but it appears that the flow develops more quickly nearer to the wing root. For the same distance traveled (see $x/c = 1.69$ for example) more leading edge vortices have formed and shed at the 1/2 span location than at 3/4 or 7/8 span. Also, as was observed previously, shed vortices tend to lift further off of the wing surface on the outboard sections.

4.1.3. Spanwise Views. Figure 13 shows the spanwise flow-field at the trailing edge of the wing and Figure 14 shows the flow in the wake, 4.2 degrees of rotation (a quarter-chord of travel at 3/4 span) behind the trailing edge. In all images, the wing is moving into the page and the suction side of the wing is to the right. Dashed lines mark the 1/2, 3/4, and 7/8 span planes.

The spanwise flow is characterized by the strong tip vortex that forms in the first 10 degrees of the wing stroke and extends into the wake. Near $\theta = 45$ deg, a large incoherent region of vorticity on the upper surface of the wing appears at 3/4 span as the shed leading edge vortices

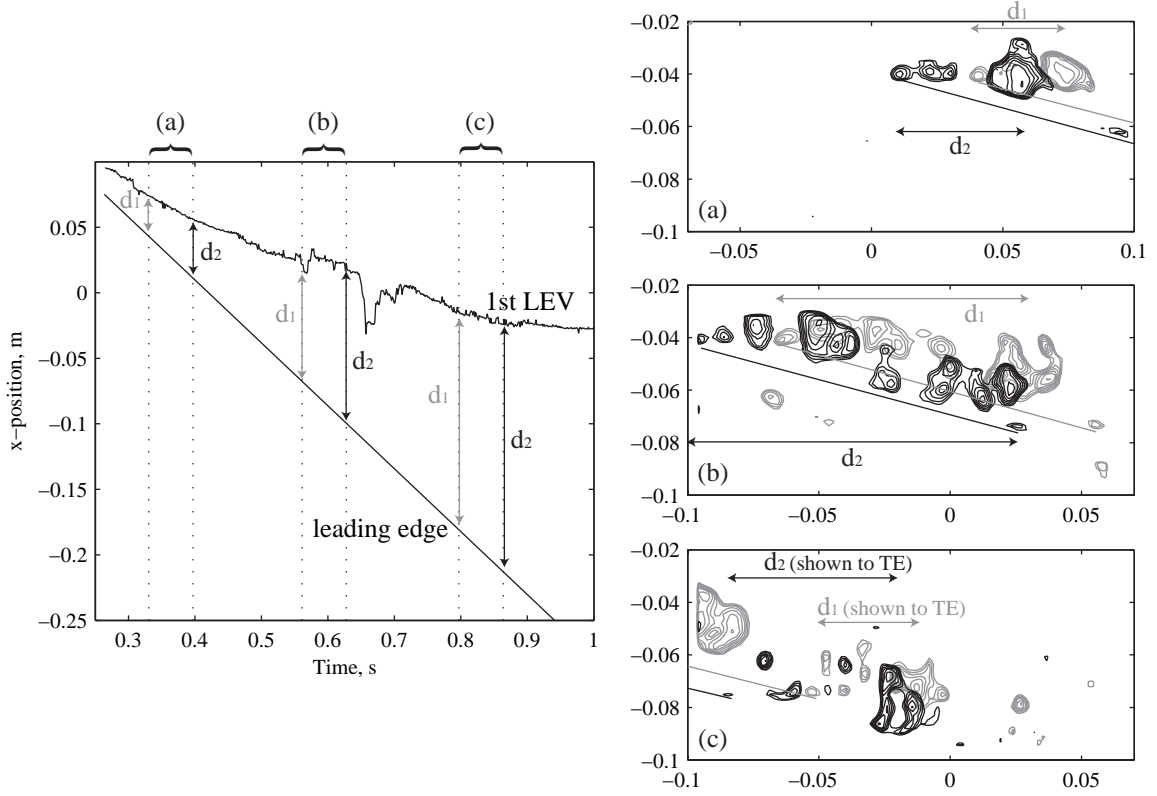


FIGURE 10. Streamwise position of the first shed leading edge vortex at 3/4 span.

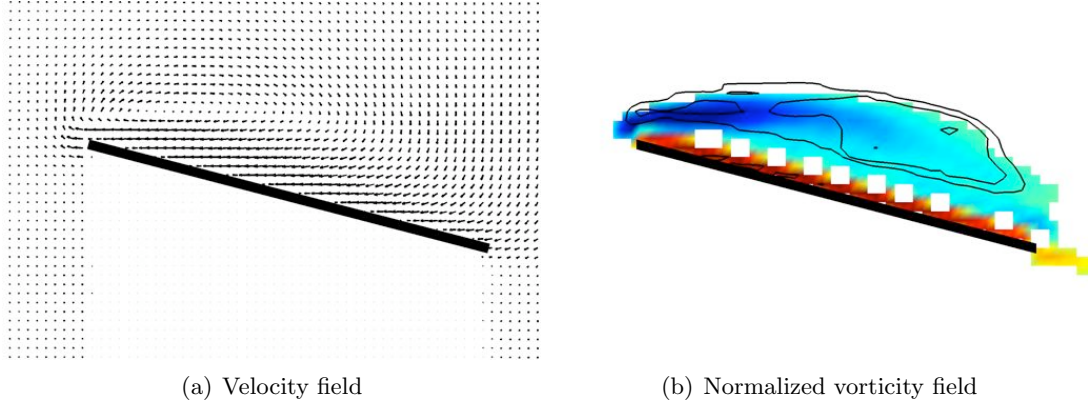


FIGURE 11. Time-averaged flow-field over 30.8 deg of the wing stroke.

reach the trailing edge (see Figure 8(k)). The same happens at $\theta = 50.85$ deg when the leading edge vortices at 7/8 span reach the trailing edge and appear in the spanwise view (Figs. 8(p) and 13(d)). This cloud of vorticity passes over the wing, ultimately forming a shear layer extending into the wake.

Figure 15 shows spanwise distributions of maximum local spanwise velocity above the wing surface normalized by the local freestream, $U' = \omega r$. There is a strong spanwise flow ($\approx 60\%$ of the freestream) from wing root to tip after a wing stroke angle of about 45 degrees which is not observed earlier in the wing stroke. In early experiments, spanwise flow was observed at 5% chord and a stroke angle of 45 degrees, so there may be significant spanwise flow earlier in the wing stroke that does not appear in these measurements due to the time required for the flow

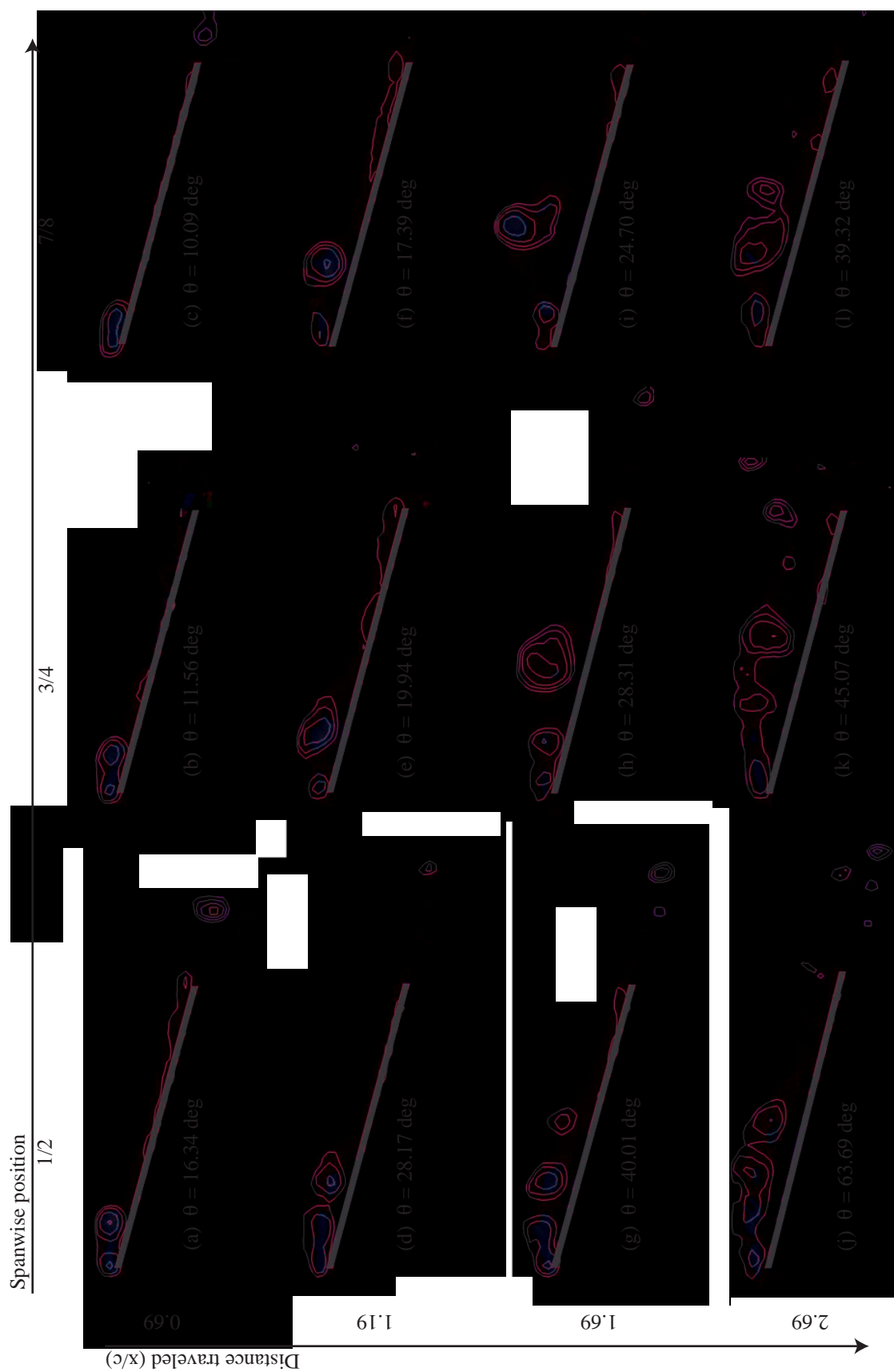


FIGURE 12. Normalized vorticity fields. Each row represents three stations on the wing after traveling equivalent x/c distances.

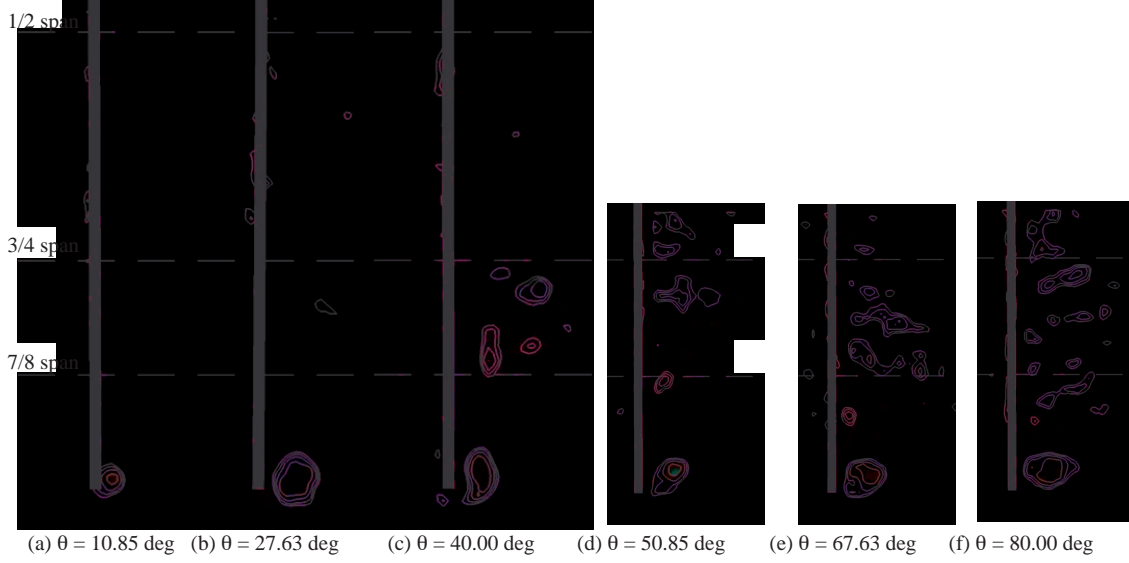


FIGURE 13. Spanwise view of the normalized vorticity field at the trailing edge.

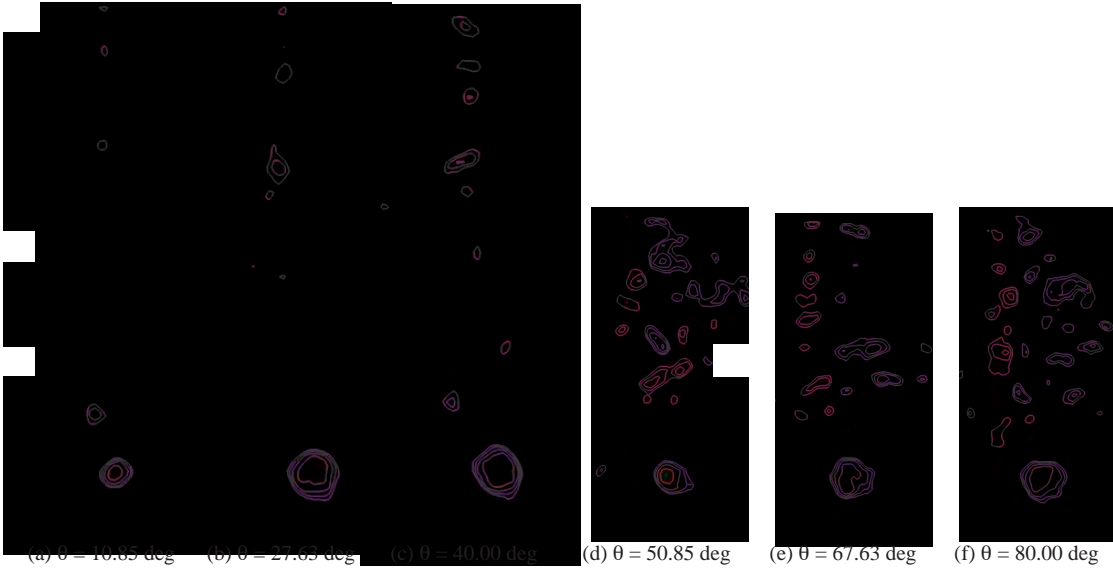


FIGURE 14. Spanwise view of the normalized vorticity field in the wake $0.25c$ behind the trailing edge.

to move from the leading edge to the trailing edge. (The light sheet was moved to the trailing edge in later experiments due to laser reflections.)

4.1.4. Force History. Unsteady force data was acquired for an 85 degree wing stroke in order to quantify the aerodynamic forces produced by the waving wing. As described previously, the force balance was mounted such that it measured the forces normal and tangential to the wing. Figure 16 shows the unsteady forces measured as a function of chord-lengths traveled at $3/4$ span. Rotating the measured forces by the angle of attack, the lift and drag coefficients are shown in Figure 17, both unfiltered and filtered and smoothed.

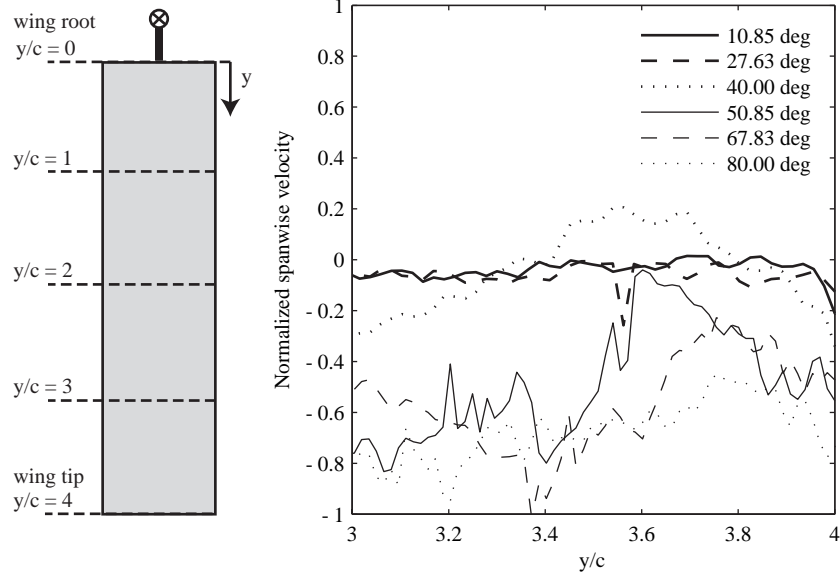


FIGURE 15. Spanwise local velocities at the trailing edge normalized by the local freestream.

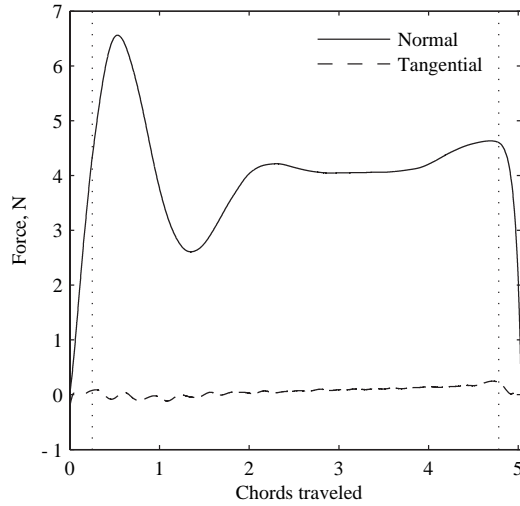


FIGURE 16. Normal and tangential forces.

The wing reaches its maximum velocity at 0.25 chord-lengths of travel as marked by the dotted line, but for the first 0.52 chord-lengths of travel (9 degrees of rotation) the lift coefficient continues to grow quickly to a maximum value of 1.43, 60% higher than the “steady-state” lift. Lift then drops to a minimum lift coefficient of 0.57 over the next chord-length of travel before eventually recovering near 2 chord-lengths of travel (34 degrees of rotation) to an intermediate “steady-state” value of 0.88. This lift is then maintained for the rest of the constant velocity portion of the wing stroke. The drag coefficient has a much lower signal to noise ratio, but the shape of the smoothed curve follows the same pattern as the lift for the reasons given above.

Figure 18 illustrates how the flow-field matches up with the measured lift-curve. Early in the wing stroke, as the lift is increasing rapidly (a), a distinct leading edge vortex is forming on the suction side of the plate and the starting vortex is visible just downstream of the trailing edge. As the lift drops off (b), the leading edge vortex has separated from the wing and is moving downstream. This vortex passes over the surface of the wing while a new leading edge vortex begins to form. The lift begins to recover (c) while vortices continue to form. When

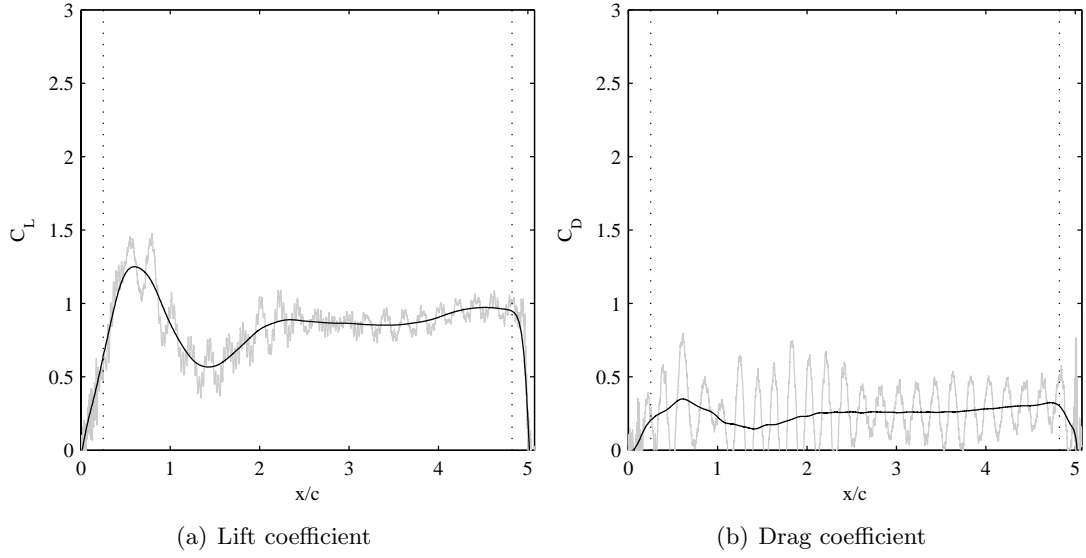


FIGURE 17. Unfiltered (grey) and filtered (black) force coefficients.

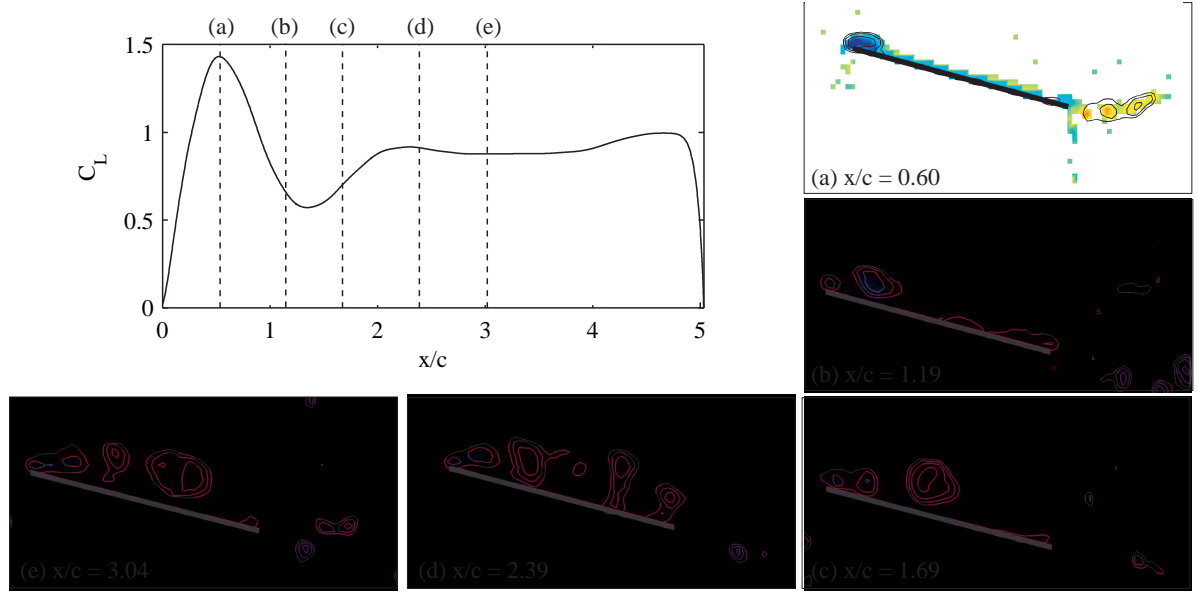


FIGURE 18. Lift coefficient versus chords traveled and vorticity field.

the lift reaches the steady-state value (d-e) several vortices coexist above the wing. After this time there is a continuous pattern of shedding vortices in a quasi-periodic fashion as described previously. This suggests that the rapid buildup of lift during the initial stages of the wing stroke is due to the development of the attached leading edge vortex and the movement of the starting vortex away from the wing.

4.1.5. Leading Edge Vortex Circulation. In order to more closely examine the behavior of the leading edge vortex, the circulation of the first leading edge vortex was computed by first finding the vorticity field $\omega = \nabla \times \mathbf{u}$ and then integrating $\Gamma = \int \omega \cdot d\mathbf{S}$ over the vortex core. Figure 19 shows the circulation of the leading edge vortex as a function of chords traveled for two definitions of the vortex core: the $\gamma = 0.6$ contour and the $\gamma = 0.7$ contour. Each data

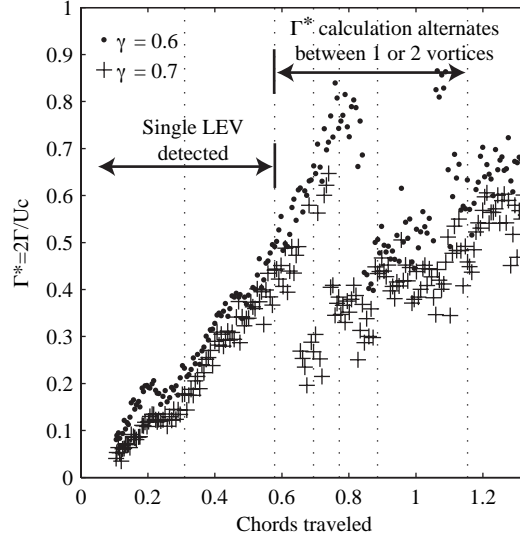


FIGURE 19. Normalized circulation computed from PIV data.

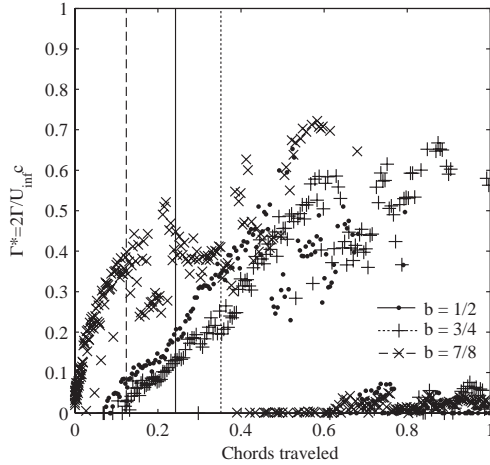


FIGURE 20. Leading edge vortex circulation at 1/2, 3/4, and 7/8 span.

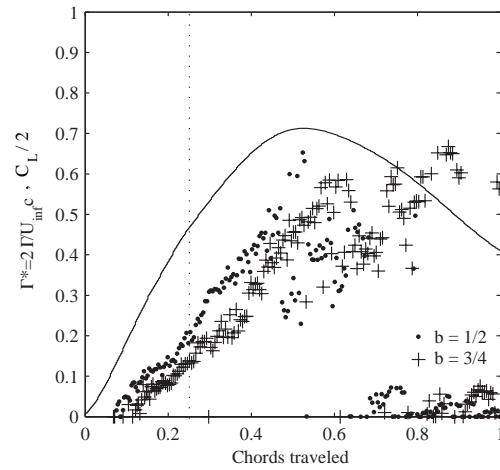


FIGURE 21. Leading edge vortex circulation and wing lift coefficient.

point on the chart was computed from a separate snapshot of the velocity field as measured using PIV.

Figure 20 shows how the growth of the leading edge vortex varies along the span as a function of local distance traveled. The vertical lines mark the shedding of the first leading edge vortex, defined by the point at which the vortex core pinches off into two separate $\gamma = 0.8$ contours. (The point at which the vortex sheds as marked in Figure 20 does not match the break-off point marked in Figure 19 because the value of Γ^* depends on the resolution of the PIV data. Figure 20 was computed using lower resolution PIV data, but is still useful for comparisons amongst data taken at the same resolution.) It is apparent that the leading edge vortex grows most quickly at 7/8 span and breaks off well before the stations farther inboard, likely due to its proximity to the tip vortex. At both 1/2 and 3/4 span the leading edge vortex sheds at $\Gamma^* \approx 0.30$, though the vortex sheds more quickly at 1/2 span.

By computing the circulation of the leading edge vortex it has been found that the initial vortex grows quickly until the point of maximum lift. Figure 21 compares the leading edge

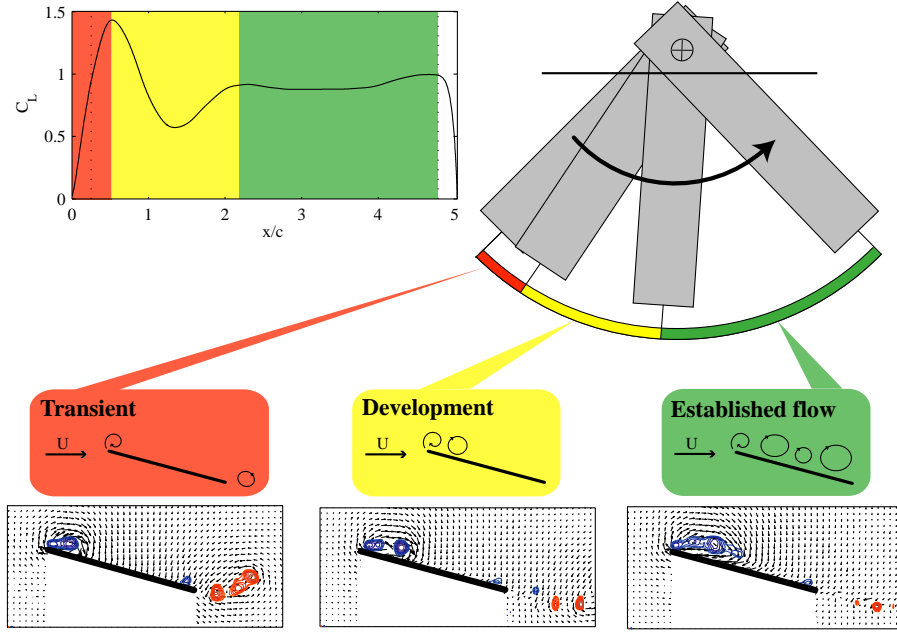


FIGURE 22. The three stages of flow development on an impulsively started waving wing: Transient, Development, and Established flow.

vortex circulation Γ^* and $C_L/2$ through the first part of the wing stroke. The normalized circulation Γ^* is suitable for comparison to the lift coefficient because rearranging the lift per unit span, $L' = \rho U \Gamma$ or $L' = \frac{1}{2} \rho U^2 c C_L$, the wing lift coefficient becomes $C_L = 2\Gamma/Uc$. Γ^* values are much lower than C_L because the leading edge vortex is not the only source of lift on the waving wing. The circulation is not computed for the first 0.1 chord-lengths of travel because the leading edge vortex is not strong enough to have a $\gamma = 0.7$ contour around which to integrate, but once the vortex is strong enough to compute Γ^* the circulation and lift coefficient grow at a very similar rate. Furthermore, the circulation values begin to jump around near between 0.5 and 0.6 chords of travel suggesting that in this region the vortex has separated from the leading edge and a second vortex is forming. The separation of the first leading edge vortex and the formation of a second vortex occur at the same point in the wing stroke as the lift peak.

4.1.6. Three Phases of Flow Development. Based on the observations presented in this section, it is proposed that the flow on a waving wing develops over three stages as illustrated in Figure 22. At the start of the wing stroke, during the initial *transient*, the flow field is characterized by the growth of a strong leading edge vortex. Flow separates at the sharp leading edge and quickly forms a leading edge vortex which remains attached to the wing. During this phase the strengthening of the leading edge vortex causes a rapid increase in lift. This phase ends when the vortex sheds and a second vortex begins to form at the leading edge.

The next flow observed on the waving wing is the *developing flow*. Flow continues to separate over the leading edge and a second leading edge vortex forms. Because the first vortex has moved downstream its effect on lift is diminished. The new leading edge vortex does not achieve the same ultimate strength before it sheds and in this phase the total lift is relatively low.

Finally, in the *established flow* phase a periodic pattern of vortex shedding from the leading edge is observed. During this phase there are multiple vortices present above the wing at all times producing a constant lift coefficient of an intermediate value.

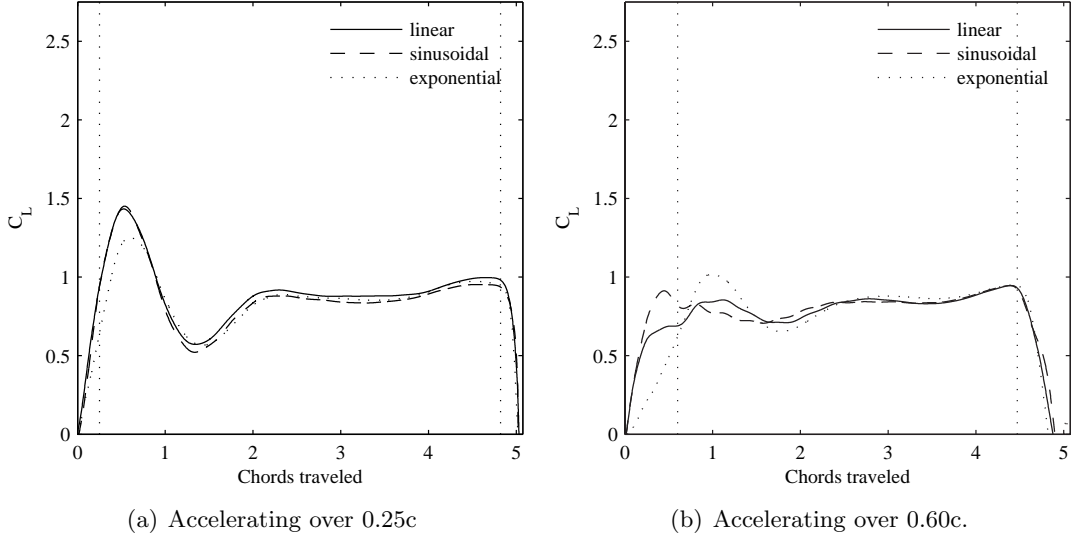


FIGURE 23. Lift coefficient for the waving wing accelerating over 0.25c and 0.60c at $Re = 60,000$, $\alpha = 15$ deg.

4.2. Effect of Wing Kinematics. The waving wing stroke was programmed using three different velocity profiles. Equations for the acceleration phase of the wing stroke are given below.

$$\begin{aligned}
 \text{exponential} \quad \omega(t) &= \frac{\omega_0}{\theta_0} \exp\left(\frac{\omega_0}{\theta_0}t + \ln \theta_0 - \frac{\omega_0 t_0}{\theta_0}\right) \\
 \text{linear} \quad \omega(t) &= \frac{\omega_0}{t_0}t \\
 \text{sinusoidal} \quad \omega(t) &= \frac{\omega_0}{2} \sin\left(\frac{\pi}{t_0}t + \frac{3\pi}{2}\right) + \frac{\omega_0}{2}
 \end{aligned}$$

The wing was accelerated such that it reached its maximum velocity after 0.10 (exponential only), 0.25, or 0.60 chord-lengths of travel at 3/4 span. For each case, the wing stroke was symmetric such that the wing decelerated in the same way before reaching a maximum stroke angle of 90 degrees.

The unsteady lift coefficients for the waving wing at $Re = 60,000$, $\mathcal{R} = 4$, and $\alpha = 15$ deg are given in Figure 23 for a variety of kinematics. The end of the wing acceleration and the start of the deceleration are marked by the vertical dotted lines. The shape of the lift-curve is similar for all three cases accelerating over 0.25c. From the start of the wing stroke there is a steep increase in lift leading to a peak, followed by a sharp drop and subsequent recovery to an intermediate level. The maximum lift coefficients for the linear, sinusoidal, and exponential velocity profiles are 1.34, 1.39, and 1.26. The steady state lift coefficient is 0.88 for all three cases.

The primary differences in the lift-curves occur near the start of the wing stroke. Past about 2.5 chord-lengths of travel (45 degrees of rotation) the steady-state lift coefficient is the same for all of the velocity profiles accelerating over both 0.25 and 0.60 chord-lengths, but in the early stages of the wing stroke the shape of the lift-curve can be affected by the time-history of the wing motion. The unsteady lift coefficients for the wing accelerating over 0.60 chord-lengths are shown in Figure 23(b). At these low accelerations both the timing and the magnitude of the lift peak depends on the time-history of the wing motion.

In Figure 24 the lift curves for different accelerations using the same velocity profile are shown together. For all three velocity profiles, the steady state lift coefficient (past 2.5 chord-lengths of travel) is the same for all accelerations tested. Acceleration over 0.10c was only achievable with

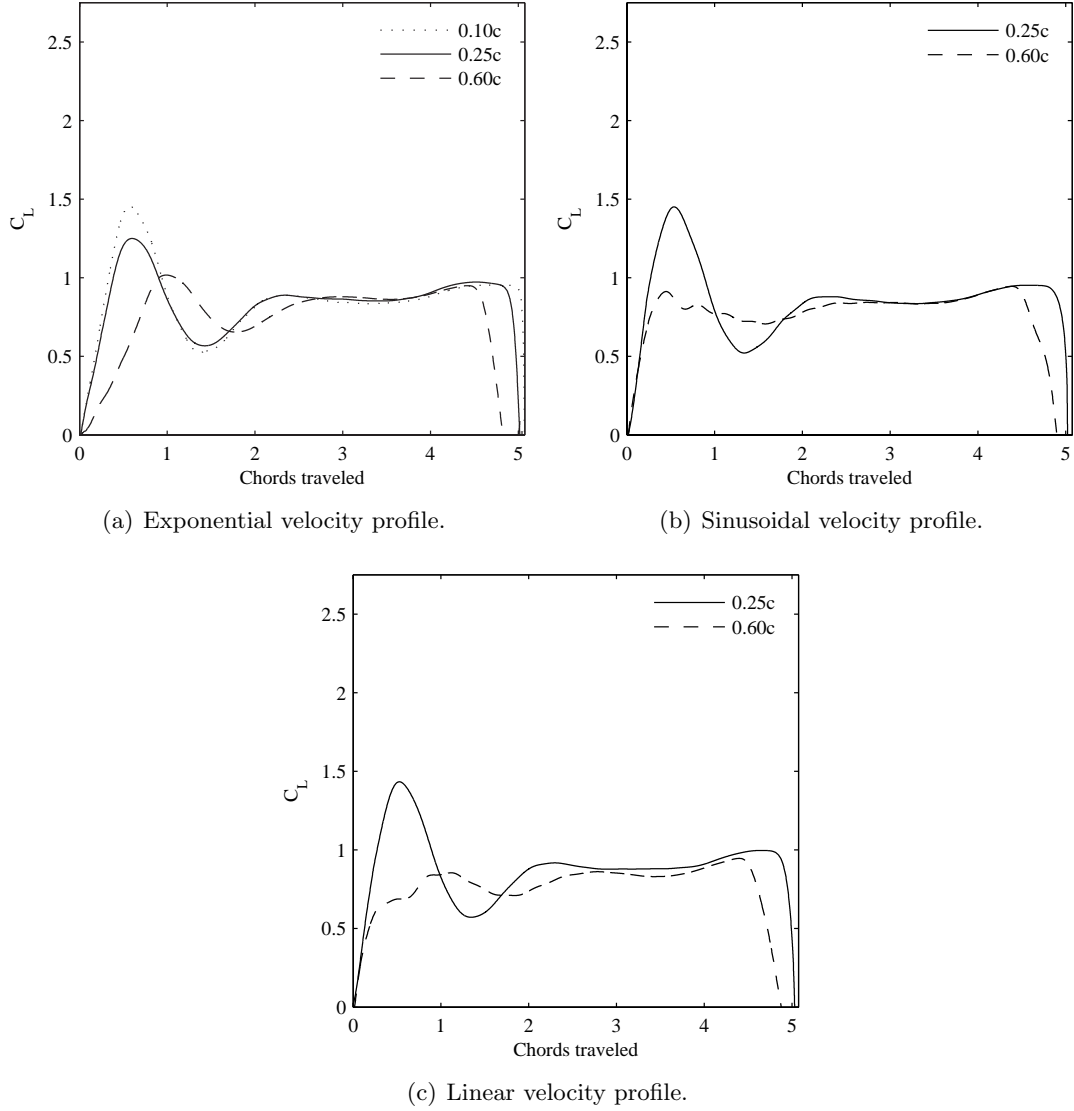


FIGURE 24. Lift coefficient for $Re=60,000$, $\alpha = 15$ deg.

the exponential velocity profile and the angular acceleration for the 0.10c case is an order of magnitude larger than the angular acceleration for the 0.25c case. Despite the large difference in inertial forces, the timing of the maximum lift peak is the same for both cases and the magnitudes are within experimental error.

Figure 25 shows Γ^* , the normalized leading edge vortex circulation, and $C_L/2$ versus time for the three exponential velocity profiles. In all three cases the shape of the Γ^* curve is similar to the lift-curve, suggesting that the growth of the leading edge vortex is related to the increase in lift. The maximum Γ^* is similar for the three cases despite differences in the maximum lift which may suggest that wing acceleration affects other sources of lift as well as leading edge vortex development.

4.3. Effect of Angle of Attack. The previous sections presented a description of the flow for a baseline case at 15 degree angle of attack. 15 degrees was selected because it is above the steady-flow stall angle and thus produces a separated flow. However, in a typical insect wing stroke the wing is at a much higher incidence during the translational phases and thus it is important to determine how the structure of the flow-field and the aerodynamic forces vary with angle of attack.

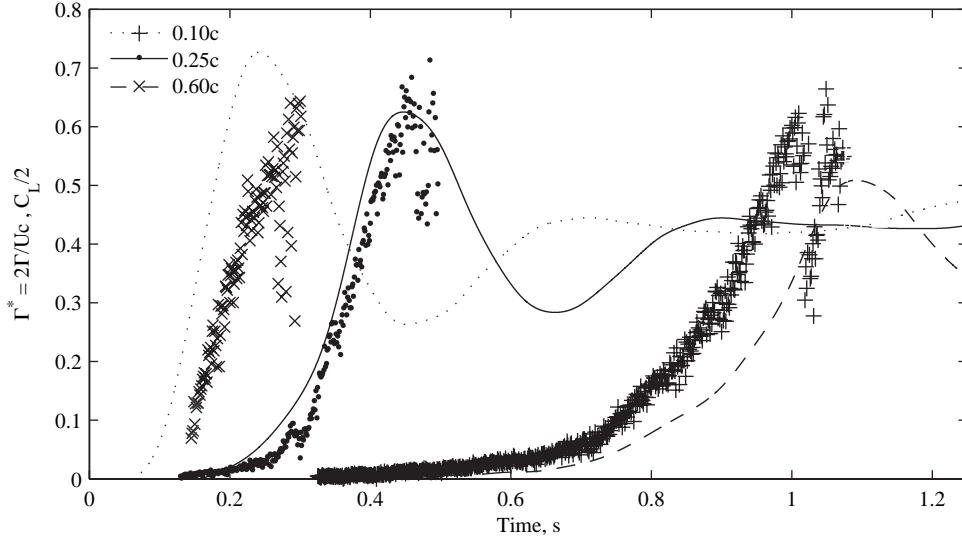


FIGURE 25. Normalized leading edge vortex circulation and lift coefficient versus time for the exponential velocity profiles accelerating over 0.10, 0.25, and 0.60 chord-lengths, $Re=60,000$, $\alpha = 15$ deg.

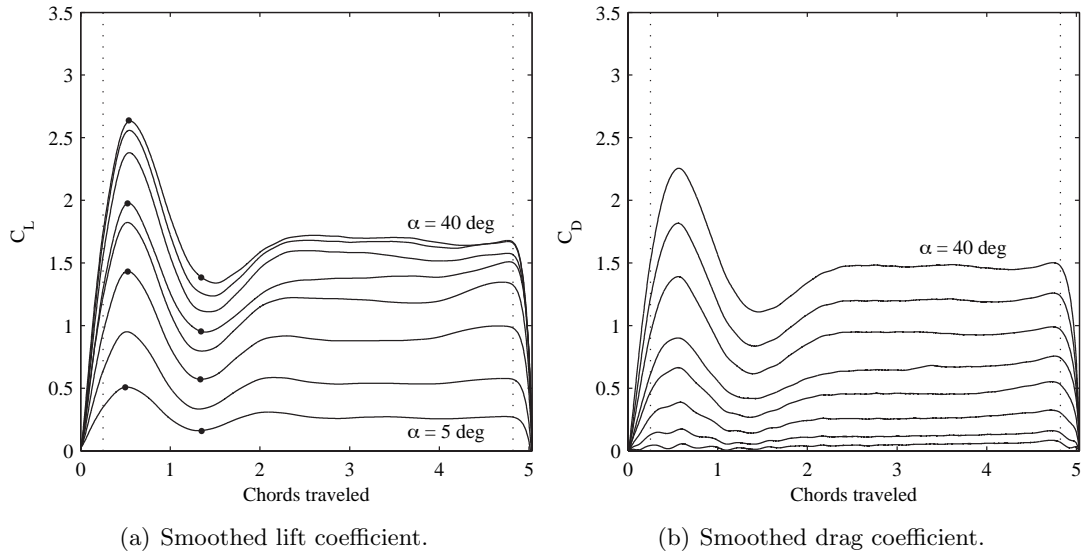


FIGURE 26. Force coefficients for $\alpha = 5, 10, 15, 20, 25, 30, 35, 40$ deg.

The unsteady lift and drag coefficients are given in Figure 26 for angles of attack between 0 and 40 degrees. The shape of the lift curve and timing of the lift peak is the same at all angles of attack tested. Lift increases with angle of attack, though increases in lift get smaller at the higher angles of attack. The shape of the drag curves are similar to the lift curves and drag increases more rapidly at high angles of attack.

Figure 27 shows the flow-field at the lift peak for a 5, 15, 25, and 40 degree angle of attack as marked in Figure 26(a). The structure of the flow development does not appear to change significantly with angle of attack. The flow is at a similar stage of development in all cases and there is a strong vortex at the leading edge. As the angle of attack increases, the leading edge vortex becomes larger and the force coefficients increase. At all of the angles of attack tested, the lift peak occurs when the first leading edge vortex is at its strongest and has not yet moved away from the leading edge. The flow-field at the minimum lift point is shown in Figure 28. At

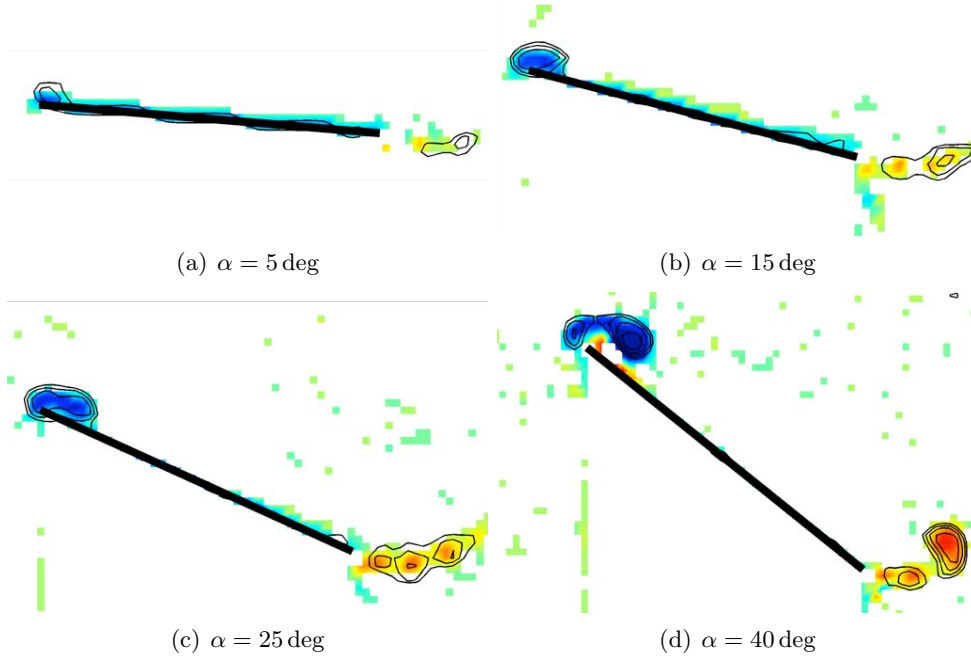


FIGURE 27. Vorticity field (at 3/4 span) at the lift peak, $x/c = 0.52$.

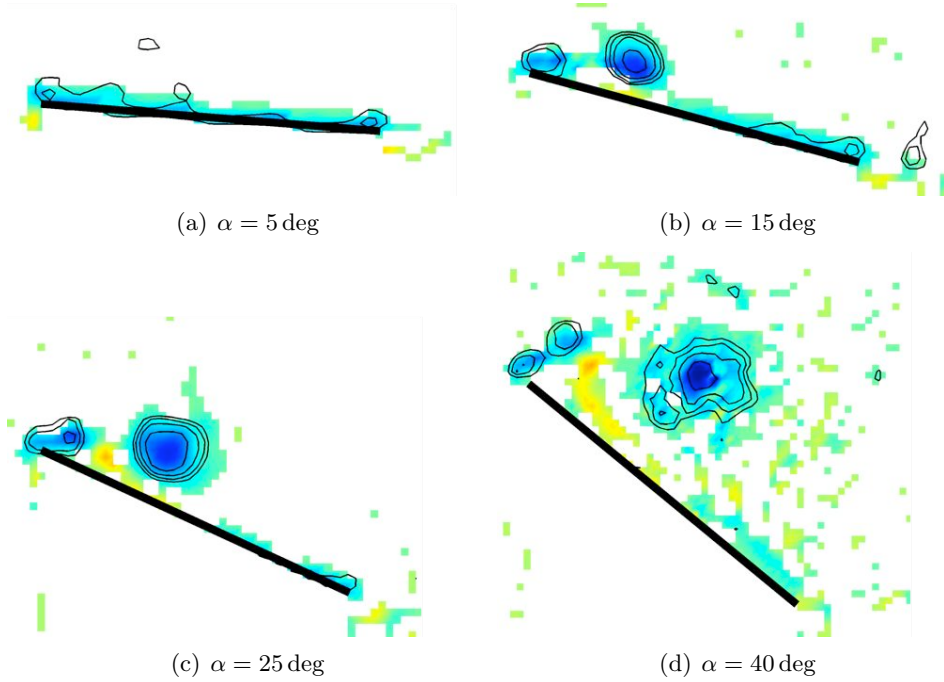
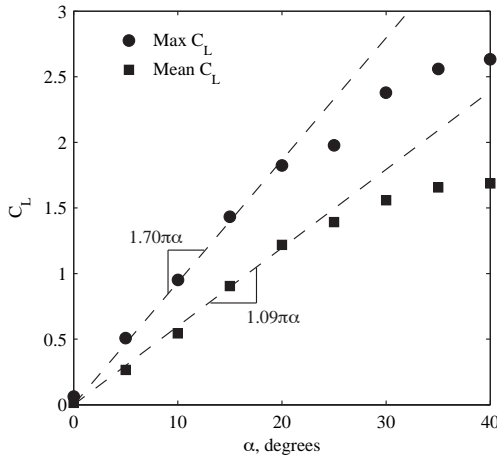


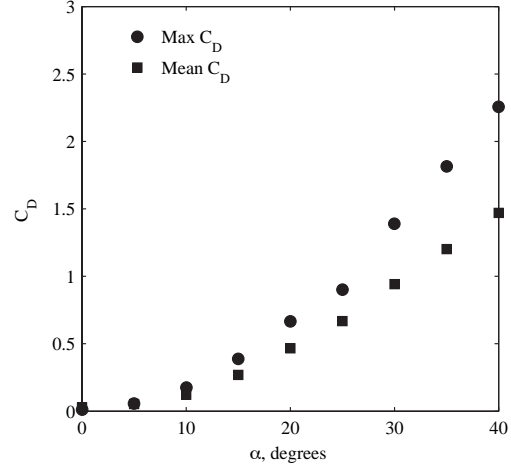
FIGURE 28. Vorticity field (at 3/4 span) at the lift minimum, $x/c = 1.40$.

this point in the wing stroke the first leading edge vortex has separated and is sitting over the wing while a second vortex forms at the leading edge.

The maximum and mean lift coefficients over the wing stroke are shown as a function of angle of attack in Figure 29. The maximum lift coefficient is the top of the transient lift peak and the mean lift coefficient is the quasi-steady value reached after about 2.5 chord-lengths of travel. Lift appears to grow linearly at low to moderate angles of attack before a gentle stall past $\alpha = 25$ deg. A linear fit for the $\alpha \leq 20$ deg results in a lift-curve slope of $1.70\pi\alpha \text{ rad}^{-1}$



(a) Lift coefficient



(b) Drag coefficient

FIGURE 29. Force coefficients as a function of angle of attack.

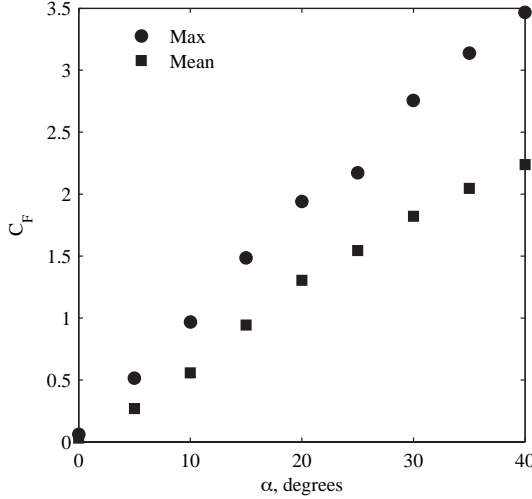


FIGURE 30. Total force coefficient.

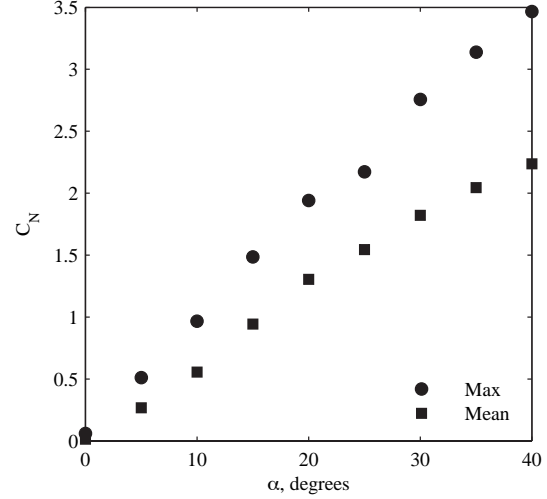


FIGURE 31. Normal force coefficient.

for $C_{L_{\max}}$ and $1.09\pi\alpha \text{ rad}^{-1}$ for the mean C_L . As expected, the drag coefficient increases with angle of attack.

If the wing stroke plane can be tilted, the total force produced by the wing can be vectored and the total force coefficient $C_F = \sqrt{C_L^2 + C_D^2}$ becomes more important. Figure 30 shows that both the maximum and mean total force coefficients increase with angle of attack and thus the largest aerodynamic forces are produced by the wing at high angle of attack. The force acting normal to the wing is given in Figure 31. Since almost all of the force produced by the waving wing acts normal to the wing C_N is very similar to C_F given in the previous figure.

4.4. Effect of Reynolds Number. The results presented thus far have all been at a Reynolds number of 60,000. This is at the high end for the current generation of micro air vehicle designs and as micro air vehicles continue to get smaller, so will the operating Reynolds number. As the Reynolds number drops, transition may affect vortex development and lift generation and an understanding of Reynolds number effects is important so that the current work can be related to previous studies at lower Reynolds numbers. Furthermore, for MAV design it is crucial to

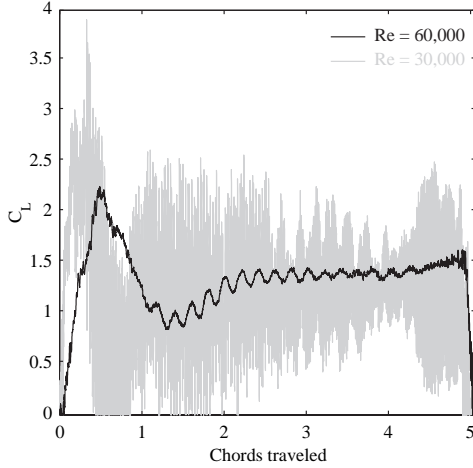


FIGURE 32. Raw lift coefficient at $\alpha = 25$ deg as a function of chords traveled.

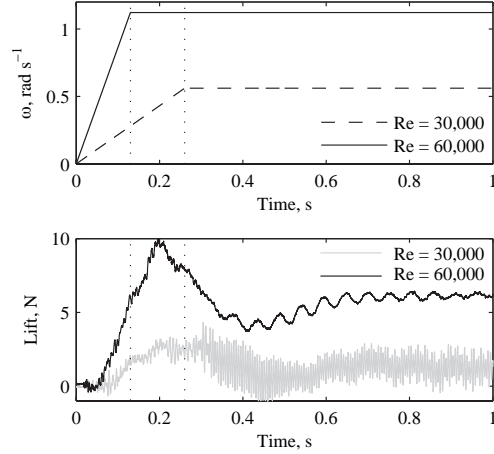


FIGURE 33. Angular velocity and raw lift force at $\alpha = 25$ deg as a function of time.

know if a “critical” Reynolds number exists for the effects observed on the waving wing. To investigate the effect of Reynolds number on the waving wing, lower Reynolds numbers were achieved by rotating the same aspect ratio 4 wing at a lower angular velocity.

Figure 32 compares the time-history of the lift coefficient at $Re = 30,000$ and $60,000$ at a 25 degree angle of attack. The raw data is shown instead of the smoothed data to make the error in the data clearer. The maximum lift coefficient is 2.27 ± 0.61 at $Re = 30,000$ and 1.98 ± 0.15 at $Re = 60,000$. Although the error makes it difficult to say much about the effect of Reynolds number on the maximum lift coefficient, the timing of the lift peak appears to be different. Lift appears to rise more quickly at $Re = 30,000$ and reaches a maximum earlier in the wing stroke than at $Re = 60,000$. This may suggest that the leading edge vortex should grow and shed more quickly at the lower Reynolds number. The angular velocity and lift force as a function of time is given in Figure 33. At $Re = 30,000$ the wing acceleration is about half of that at $Re = 60,000$ and it takes a longer time to reach the steady state velocity. The build-up of lift over time is similar at the two Reynolds numbers, but since the wing is moving more slowly at $Re = 30,000$ the lift peak occurs after a smaller number of chord-lengths traveled. The lift peaks occur at similar absolute times rather than a non-dimensional time.

Figure 34 compares the flow-field at the three Reynolds numbers and a wing stroke angle of 10.85 degrees ($x/c = 0.65$), past the lift peak for all three cases. The distance from the leading edge to the shed vortex is found to increase with decreasing Reynolds number. This is consistent with the previous observations and suggests that the leading edge vortex grows even faster at $Re = 10,000$.

The growth of the leading edge vortex is quantified as $\Gamma^* = 2\Gamma/Uc$ in Figure 35 where Γ is the circulation of the leading edge vortex found by integrating around the $\gamma = 0.7$ contour. It can be seen that the vortex grows more quickly at lower Reynolds number. The vertical lines indicate the point at which the vortex breaks off of the wing. (Note that the timing of the vortex break-off does not match the timing of the lift peak because the PIV data used to calculate Γ^* for these cases is of a relatively low resolution and the predicted vortex shedding point is very sensitive to this as discussed in Section 3.5.) Vortex break-off occurs significantly earlier at $Re = 30,000$ than at $Re = 60,000$ which is consistent with the earlier lift peak observed in the force measurements, and even earlier still at $Re = 10,000$. This suggests that the timing of the lift peak is dependent on Reynolds number. It is possible that at higher Reynolds numbers the vortex grows stronger and is thus able to stay attached to the wing longer, but this would suggest that the vortex would reach a higher Γ^* value before break-off. In fact, at each Reynolds

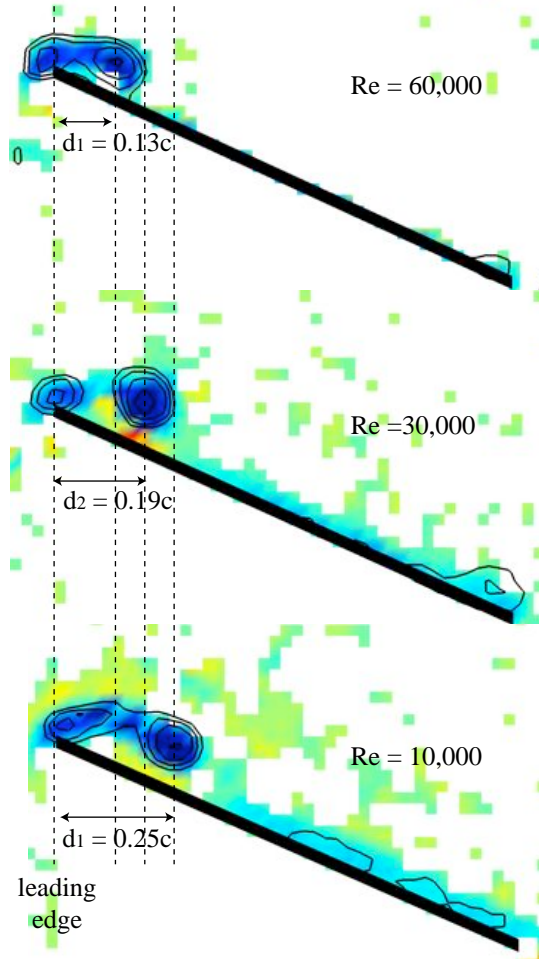


FIGURE 34. Normalized vorticity fields at 3/4 span, $\theta = 10.85$ deg, $x/c = 0.65$, $\alpha = 25$ deg.

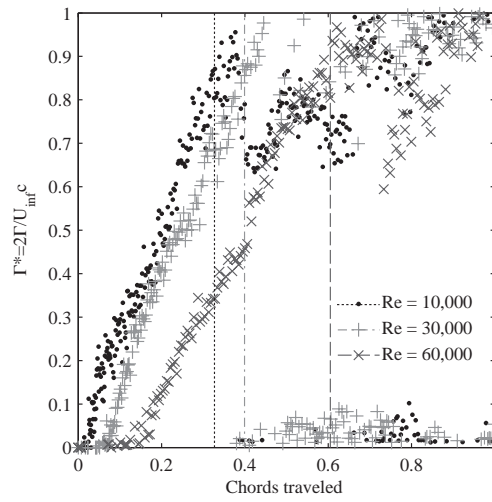


FIGURE 35. Leading edge vortex circulation at 3/4 span, $\alpha = 25$ deg.

number tested the vortex breaks off near the same value of $\Gamma^* \approx 0.88$. The observation that the vortex sheds near the same value at all three Reynolds numbers suggests that there may be some non-dimensional parameter governing vortex break-off similar to the formation number of vortex rings.

4.5. Effect of Aspect Ratio. The waving wing experiment has been performed with variations in wing kinematics, angle of attack, and Reynolds number. Through all of these variations the fundamental structure of the flow has not changed. In all of the experiments a leading edge vortex has formed early in the wing stroke but quickly shed. The attached leading edge vortex observed on insect wings is a fundamentally three-dimensional flow structure and is thought to be stabilized by some combination of the spanwise flow generated on a rotating wing and the angular accelerations present at low Rossby number. The waving wing experiments presented thus far have all been conducted with an aspect ratio 4 wing at a Rossby number of about 4.4. Insect wings, on which attached leading edge vortices have been observed, typically have lower aspect ratios, thus the waving wing experiments were repeated with an aspect ratio 2 wing ($Ro \approx 2.4$).

The angular velocity of the waving wing is directly related to the aspect ratio by $\omega = \nu Re/rc$ where $r = \frac{3}{4}Rc + r_r$ and r_r is the distance from the axis of rotation to the wing root. Since r_r is small, the rotational velocity required to achieve a given Reynolds number on the aspect ratio 2 wing is approximately twice that for the aspect ratio 4 wing. The lower aspect ratio wing is expected to have a steeper spanwise velocity gradient because higher angular velocities are required to achieve the same local Reynolds number. Also, the tip vortex will affect a greater percentage of the wingspan further increasing the three-dimensionality of the flow.

The normalized vorticity fields are shown for the aspect ratio 2 wing at $Re = 60,000$ and $\alpha = 15$ in Figure 36. The fundamental structure of the flow-field appears to be the same as at aspect ratio 4. Although the flow over the aspect ratio 2 wing is expected to be more three-dimensional, a stable attached leading edge vortex is not observed. A vortex forms along the leading edge early in the wing stroke and sheds within the first 17 degrees of rotation. This vortex moves downstream over the wing as another vortex forms and later sheds, forming a line of shed vortices extending downstream over the wing. The shed vortices move downstream though the wing stroke but have not yet reached the trailing edge of the wing at $\theta = 38.50$ deg. Vortices tend to spread further apart nearer the wing tip. This is most obvious between 1/2 and 3/4 span as shown in Figures 36(g-h). As on the higher aspect ratio wing, the shed vortices tend to lift off the wing surface near the wing tip, but remain close to the surface further inboard.

Spanwise views of the normalized vorticity field at the trailing edge and in the wake are given in Figure 37. At $\alpha = 15$ deg, a tip vortex is observed from $\theta = 17.42$ deg and persists into the wake through 78.50 degrees of rotation. Near this point in the stroke a cloud of incoherent vorticity appears between 3/4 and 7/8 span, most likely the shed leading edge vortices reaching the trailing edge.

Despite the increased three-dimensionality of the lower aspect ratio wing a stably attached leading edge vortex is not observed on the waving wing. The structure of the flow-field on the aspect ratio 2 wing is not significantly different from that at aspect ratio 4 though the tip vortex appears to be stronger.

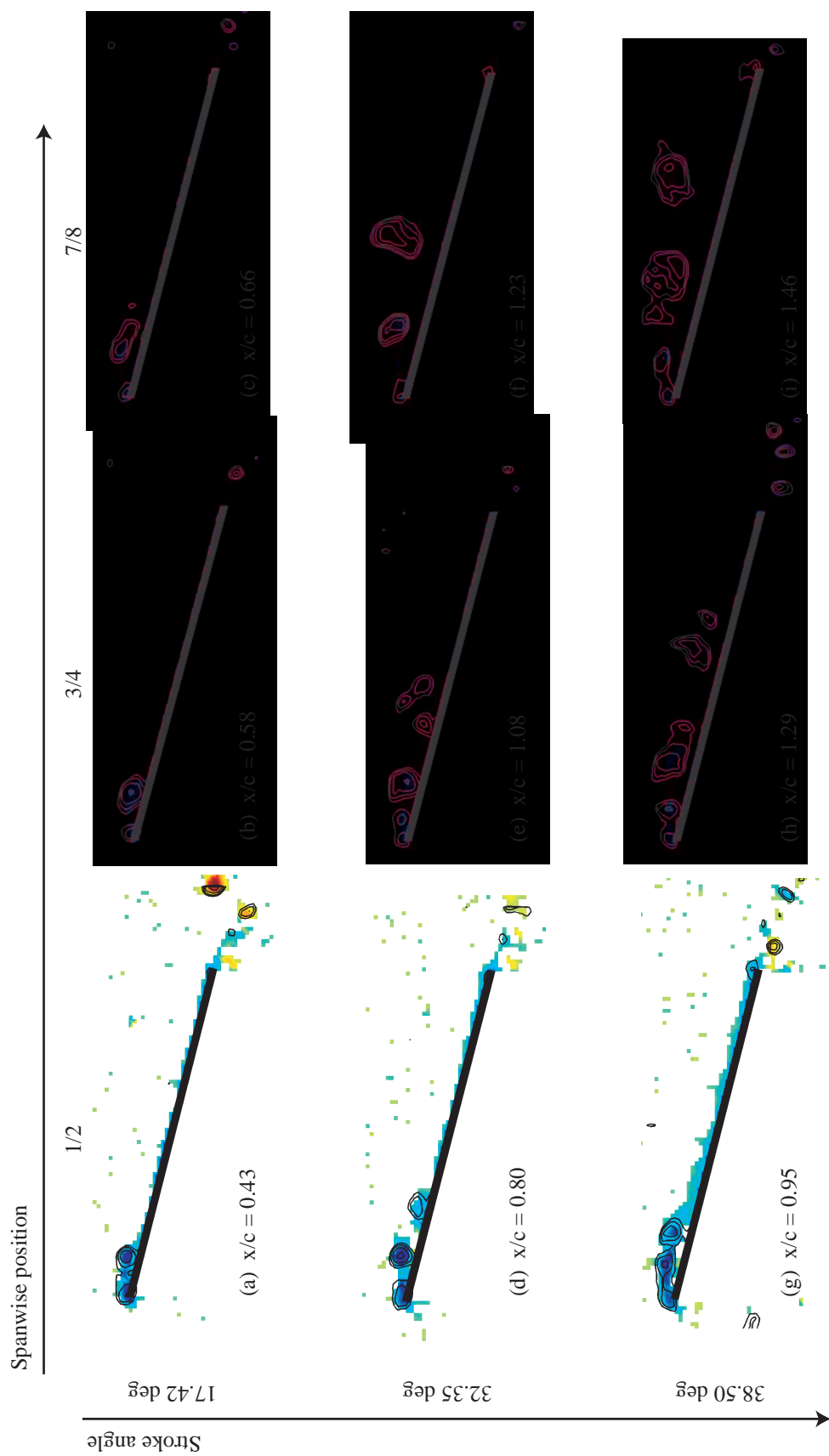


FIGURE 36. Normalized vorticity field for $AR = 2$, $Re = 60,000$, $\alpha = 15$ deg. Each row represents the three stations on the wing at an instant in the wing stroke.

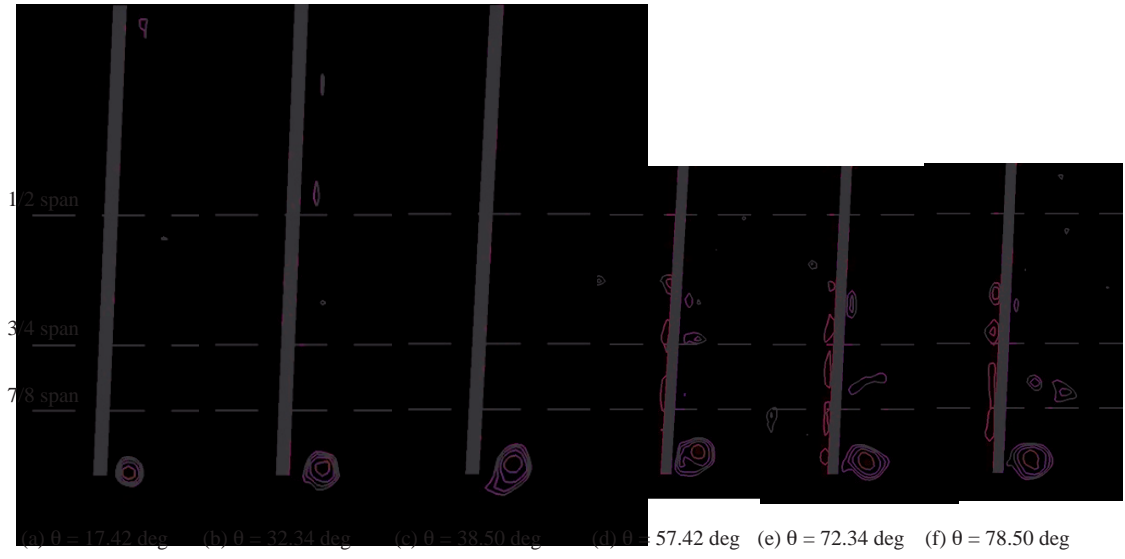


FIGURE 37. Spanwise view of normalized vorticity field at the trailing edge for $AR = 2$, $Re = 60,000$, $\alpha = 15 \text{ deg}$.

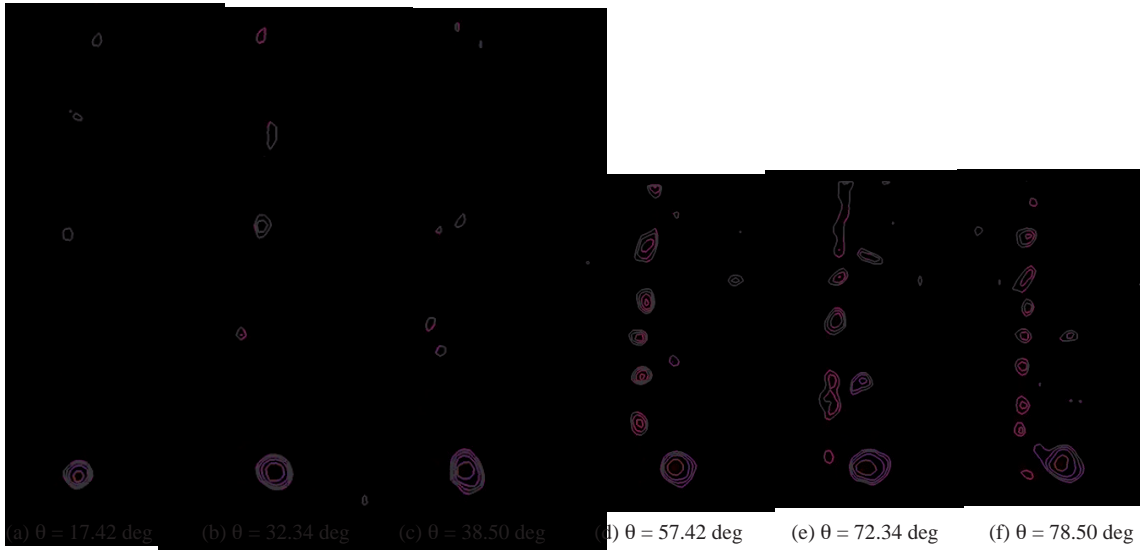


FIGURE 38. Spanwise view of the normalized vorticity field in the wake $0.25c$ behind the trailing edge for $AR = 2$, $Re = 60,000$, $\alpha = 15 \text{ deg}$.

5. CONCLUSIONS

The Waving Wing Experiment. A typical insect wing stroke is a figure-eight pattern consisting of two translational phases during which the wing rotates about the root at a constant angle of attack and two rotational phases in which the wing rapidly changes pitch. Three characteristics of the wing stroke are thought to be critical for lift generation: three-dimensionality in both geometry and kinematics, wing rotation about the root, and acceleration and deceleration over a short wing stroke. The waving wing experiment is a new experimental setup developed to be the simplest experiment that preserves the three-dimensionality, wing rotation, and unsteadiness of the insect wing stroke. The wing is quickly accelerated from rest in a rotational motion about the wing root in order to produce a fully three-dimensional unsteady flow-field.

Experiments have been performed on flat plate wings in unsteady rotation at Reynolds numbers between 10,000 and 60,000 with a focus on the development of lift during the early part of the wing stroke. Unsteady force measurements and high-speed particle image velocimetry have been used to both qualitatively and quantitatively study the formation of flow structures and the time-history of the forces produced. Several sets of wing kinematics have been tested including linear, sinusoidal, and exponential (in time) velocity profiles accelerating to the maximum velocity in 0.10, 0.25, and 0.60 chord-lengths of travel at $3/4$ span. The wing angle of attack was varied between 5 and 45 degrees for both an aspect ratio 2 and 4 wing. The flow-field was analyzed using a non-local vortex detection scheme and the computed vorticity field and the growth of the leading edge vortex was quantified by computing the circulation of the vortex as a function of time.

Flow Development on a Waving Wing. The time-history of lift force on a waving wing is characterized by a high transient lift peak followed by a steep drop and subsequent recovery to an intermediate value for all angles of attack, aspect ratios, and motion histories tested. The formation of a leading edge vortex was observed from the start of the wing stroke. This leading edge vortex did not remain attached, but rather shed from the wing within the first chord-length of travel (at $3/4$ span) and subsequently moved downstream over the wing. After the first vortex separated from the leading edge, subsequent vortices continued to form and shed from the leading edge creating a series of vortices extending over the wing surface.

The circulation of the leading edge vortex was computed from the velocity field as measured using particle image velocimetry. The lift peak was found to occur at the same time that the first leading edge vortex breaks off of the wing and a second vortex begins to form at the leading edge. These results suggest that the transient lift peak is related to the leading edge vortex behavior. The rise in lift to the peak is related to the growth of the leading edge vortex and the subsequent lift drop-off is due to vortex shedding. Leading edge vortex shedding was observed on both the aspect ratio 2 and 4 wings.

It is proposed that the flow on an impulsively started waving wing develops over three stages:

Transient: As the wing begins to accelerate, flow separates at the sharp leading edge and quickly forms a vortex which remains attached to the wing. During this phase the strengthening of the leading edge vortex causes a rapid increase in lift. The transient phase ends when this first leading edge vortex separates from the wing, begins to move downstream, and a second vortex begins to form.

Development: During the developing flow lift values are low as flow continues to separate at the leading edge and the second vortex grows.

Established Flow: In the established flow a periodic pattern of vortex shedding is observed. During this phase there are typically three to four vortices present above the wing at all times and the lift coefficient remains constant at an intermediate value.

Spanwise particle image velocimetry revealed a strong tip vortex that forms within the first 10 degrees of rotation and persists through the wing stroke. A spanwise flow of the same order of magnitude as the chordwise flow over the wing was observed after a stroke angle of 45 degrees. The structure of the flow-field was found to be similar along the wing span. High aspect ratio

leading edge vortices extending along the length of the wing were observed to form and shed, forming a periodic pattern of vortex shedding as described above.

The development and ultimate strength of the leading edge vortex can be influenced by the wing's acceleration. Force histories show that if the wing experiences a sufficiently high acceleration, the lift force produced is not affected by the wing's velocity profile. However, if the wing experiences a low acceleration at the start of the wing stroke then the time-history of the wing's velocity can affect both the magnitude and timing of the lift peak. The shape of the lift-curve and timing of the lift peak were not significantly altered by angle of attack between 0 and 45 degrees. The circulation of the leading edge vortex grows more quickly at Reynolds numbers 10,000 and 30,000 than it does at 60,000.

Relevance to the Design of Flapping Wing Micro Air Vehicles. A leading edge vortex was observed to form on a waving wing but quickly separated from the leading edge. The development of this unstable leading edge vortex produces a high lift transient very similar to that observed by others at lower Reynolds numbers in a flow with a stably attached leading edge vortex. This suggests that a leading edge vortex does not have to be stably attached to the wing to produce a high lift coefficient, thus it may not be important to design a wing specifically to maintain an attached leading edge vortex.

The flow structures on the waving wing and the resulting time-history of lift is similar across a range of angles of attack. This allows angle of attack to be selected for optimum force production without constraints imposed by fundamental changes in the flow-field.

Despite the highly three-dimensional nature of the wing geometry and kinematics, spanwise variations in the flow are relatively small and wing aspect ratio may be selected for maximum force production or other considerations such as size and weight.

The magnitude and timing of the high lift peak can be affected by the wing kinematics for low accelerations. The maximum lift peak was produced with high wing accelerations, and at high accelerations the time-history of the wing velocity has no effect on force production. This may simplify the design of flapping wing mechanisms by allowing for simple wing motions, albeit at relatively quick accelerations.

PUBLICATIONS

Jones, A. R., Pitt Ford, C. W., and Babinsky, H., "Three-Dimensional Effects on Sliding and Waving Wings," in preparation for *Journal of Aircraft*.

Jones, A. R. and Babinsky, H., "Reynolds Number Effects on Leading Edge Vortex Development on a Waving Wing," submitted to *Experiments in Fluids*.

Pitt Ford, C. W., Jones, A. R., and Babinsky, H., "Low Reynolds Number Study of Wings for Micro-Air Vehicles," in the Royal Aeronautical Society Aerodynamics Conference, University of Bristol, United Kingdom, July 27-28, 2010.

Jones, A. R., Unsteady Low Reynolds Number Aerodynamics of a Waving Wing, PhD thesis, University of Cambridge, 2010.

Jones, A. R. and Babinsky, H., "Unsteady Lift Generation on Rotating Wings at Low Reynolds Numbers," *Journal of Aircraft*, Vol. 47, May-June 2010, pp. 1013-1021.

Jones, A. R. and Babinsky, H., "Three-Dimensional Effects on a Waving Wing," AIAA Paper 2010-0551 in the 48th AIAA Aerospace Sciences Meeting and Exhibit, Orlando, Florida, Jan. 4-7, 2010.

Beckwith, R. M. H. and Babinsky, H., "Impulsively Started Flat Plate Flow," *Journal of Aircraft*, Vol. 46, Nov.-Dec. 2009, pp. 2186-2188.

Babinsky, H. and Jones, A. R., “Unsteady Lift Generation on Sliding and Rotating Flat Plate Wings,” invited AIAA Paper 2009-3689 in the 39th AIAA Fluid Dynamics Conference, San Antonio, Texas, June 22-25, 2009.

Jones, A. R. and Babinsky, H., “Three-Dimensional Waving Wings at Low Reynolds Numbers,” AIAA Paper 2009-0790 in the 47th AIAA Aerospace Sciences Meeting and Exhibit, Orlando, Florida, Jan. 5-8, 2009.

Beckwith, R. M. H., *Impulsively Started Flat Plate Wing*, MPhil thesis, University of Cambridge, 2008.

REFERENCES

- [1] R. BECKWITH AND H. BABINSKY, *Impulsively started flat plate flow*, Journal of Aircraft, 46 (2009), pp. 2186–2188.
- [2] —, *Impulsively started flat plate wing*, in 47th AIAA Aerospace Sciences Meeting and Exhibit, AIAA 2009-0789, Orlando, FL, 5-8 January 2009.
- [3] J. M. BIRCH AND M. H. DICKINSON, *Spanwise flow and the attachment of the leading-edge vortex on insect wings*, Nature, 412 (2001), pp. 729–733.
- [4] J. M. BIRCH, W. B. DICKSON, AND M. H. DICKINSON, *Force production and flow structure of the leading edge vortex on flapping wings at high and low Reynolds numbers*, Journal of Experimental Biology, 207 (2004), pp. 1063–1072.
- [5] R. DUDLEY, *The Biomechanics of Insect Flight*, Princeton University Press, 2000.
- [6] J. D. ELDREDGE, C. WANG, AND M. V. OL, *A computational study of a canonical pitch-up, pitch-down wing maneuver*, in 39th AIAA Fluid Dynamics Conference, AIAA 2009-3687, San Antonio, TX, 22-25 June 2009.
- [7] C. P. ELLINGTON, *The aerodynamics of hovering insect flight, III. Kinematics*, Philosophical Transactions of the Royal Society of London, Series B, Biological Sciences, 305 (1984), pp. 41–78.
- [8] C. P. ELLINGTON, C. VAN DEN BERG, A. P. WILLMOTT, AND A. L. R. THOMAS, *Leading-edge vortices in insect flight*, Nature, 384 (1996), pp. 626–630.
- [9] L. GRAFTIEAUX, M. MICHARD, AND N. GROSJEAN, *Combining PIV, POD and vortex identification algorithms for the study of unsteady turbulent swirling flows*, Measurement Science and Technology, 12 (2001), pp. 1422–1429.
- [10] J. JEONG AND F. HUSSAIN, *On the identification of a vortex*, Journal of Fluid Mechanics, 285 (1995), pp. 69–94.
- [11] A. R. JONES AND H. BABINSKY, *Unsteady lift generation on rotating wings at low Reynolds numbers*, Journal of Aircraft, 47 (2010), pp. 1013–1021.
- [12] D. LENTINK AND M. H. DICKINSON, *Rotational accelerations stabilize leading edge vortices on revolving fly wings*, Journal of Experimental Biology, 212 (2009), pp. 2705–2719.
- [13] T. MAXWORTHY, *Experiments on the Weis-Fogh mechanism of lift generation by insects in hovering flight, I. Dynamics of the ‘fling’*, Journal of Fluid Mechanics, 93 (1979), pp. 47–63.
- [14] G. R. NOLAN, *Aerodynamics of Vortex Lift in Insect Flight*, PhD, University of Cambridge, September 2004.
- [15] M. OL, *Vortical structures in high frequency pitch and plunge at low Reynolds number*, in 37th AIAA Fluid Dynamics Conference and Exhibit, vol. AIAA 2007-4233, Miami, FL, 25 - 28 June 2007.
- [16] M. RAFFEL, C. E. WILLERT, AND J. KOMPENHANS, *Particle Image Velocimetry: A Practical Guide*, Springer, 1998.
- [17] M. RAMASAMY AND J. G. LEISHMAN, *Phase-locked particle image velocimetry measurements of a flapping wing*, Journal of Aircraft, 43 (2006), pp. 1867–1875.

- [18] M. J. TARASCIO, M. RAMASAMY, I. CHOPRA, AND J. G. LEISHMAN, *Flow visualization of micro air vehicle scaled insect-based flapping wings*, Journal of Aircraft, 42 (2005), pp. 385–390.
- [19] J. TOOMEY AND J. D. ELDREDGE, *Numerical and experimental study of the fluid dynamics of a flapping wing with low order flexibility*, Physics of Fluids, 20 (2008).
- [20] J. R. USHERWOOD AND C. P. ELLINGTON, *The aerodynamics of revolving wings: I. Model hawkmoth wings*, Journal of Experimental Biology, 205 (2002), pp. 1547–1564.
- [21] C. VAN DEN BERG AND C. P. ELLINGTON, *The three-dimensional leading-edge vortex of a “hovering” model hawkmoth*, Philosophical Transactions of the Royal Society of London, Series B, Biological Sciences, 352 (1997), pp. 329–340.
- [22] ———, *The vortex wake of a “hovering” model hawkmoth*, Philosophical Transactions of the Royal Society of London, Series B, Biological Sciences, 352 (1997), pp. 317–328.
- [23] P. C. WILKINS AND K. KNOWLES, *The leading-edge vortex and aerodynamics of insect-based flapping-wing micro air vehicles*, The Aeronautical Journal, 113 (2009), pp. 253–262.